

ATMOSPHERE-INTERIOR EXCHANGE ON HOT ROCKY EXOPLANETS

EDWIN S. KITE

University of Chicago, Chicago, IL 60637, USA;
kite@uchicago.edu

BRUCE FEGLEY JR.

Planetary Chemistry Laboratory, McDonnell Center for the Space Sciences & Department of Earth & Planetary Sciences,
Washington University, St Louis MO 63130.

LAURA SCHAEFER

Harvard-Smithsonian Center for Astrophysics, Cambridge, MA 02138, USA.

AND

ERIC GAIDOS

University of Hawaii at Manoa, Honolulu, HI 96822, USA.

Draft version June 23, 2016

ABSTRACT

We provide estimates of atmospheric pressure and surface composition on short-period rocky exoplanets with dayside magma pools and silicate vapor atmospheres. Atmospheric pressure tends toward vapor-pressure equilibrium with surface magma, and magma-surface composition is set by the competing effects of fractional vaporization and surface-interior exchange. We use basic models to show how surface-interior exchange is controlled by the planet’s temperature, mass, and initial composition. We assume that mantle rock undergoes bulk melting to form the magma pool, and that winds flow radially away from the substellar point. With these assumptions, we find that: (1) atmosphere-interior exchange is fast when the planet’s bulk-silicate FeO concentration is low, and slow when FeO concentration is high; (2) magma pools are compositionally well-mixed for substellar temperatures $\lesssim 2400$ K, but compositionally variegated and rapidly variable for substellar temperatures $\gtrsim 2400$ K; (3) currents within the magma pool tend to cool the top of the solid mantle (“tectonic refrigeration”); (4) contrary to earlier work, many magma planets have time-variable surface compositions.

Subject headings: planets and satellites: terrestrial planets — planets and satellites: physical evolution — planets and satellites: surfaces — planets and satellites: individual (Kepler-10 b, CoRoT-7 b, KIC 12557548 b, KOI-2700 b, K2-22 b, K2-19 d, WD 1145+017, 55 Cnc e, HD 219134 b, Kepler-36 b, Kepler-78 b, Kepler-93 b, WASP-47 e).

1. INTRODUCTION

Over one hundred exoplanets have masses or radii in the rocky-planet range, and substellar equilibrium temperatures hot enough to melt peridotite rock.¹ These molten surfaces are tantalizing because they are relatively easy to detect and characterize (Rouan et al. 2011; Demory 2014; Samuel et al. 2014; Sheets & Deming 2014) - what sets molten-surface composition?

The melt-coated dayside is exposed to intense EUV irradiation, sufficient to remove H₂ (Valencia et al. 2010; Owen & Wu 2013; Lopez & Fortney 2014) and to maintain a thin silicate atmosphere (Fig. 1). In the case where all atmophile elements (e.g. C, H) have been

removed, thin-silicate-atmosphere composition is set by silicate-surface composition. Unlike the easier-to-observe nebular-accreted atmospheres and outgassed secondary-volatile atmospheres, thin exoplanetary silicate atmospheres are only now coming into view (Forget & Lecote 2014). The most-volatile rock-forming constituents of the melt (e.g. Na, K, Fe) preferentially partition into the atmosphere – fractional vaporization. Borne by winds, these volatiles make a one-way trip to the permanent nightside (Makarov & Efroimsky 2013; Callegari & Rodríguez 2013), or are lost to space (Fig. 1) – trans-atmospheric distillation. If trans-atmospheric distillation is faster than mass recycling between the melt pool and the solid interior, then surface composition will differ from bulk-planet silicate composition. But if mass recycling between the melt pool and solid interior is fast, then surface composition will be repeatedly reset towards bulk-planet silicate composition (Fig. 1).

In the first (compositionally evolved) case, with relatively slow recycling, loss of volatiles (Na, K, Fe ...) creates enriches the residue in Ca and Al, forming a refractory lag (Léger et al. 2011) (Fig. 2). The lag protects the vulnerable volatile-rich interior, as on a comet. After lag formation, atmospheric pressure is usually $\lesssim O(1)$

¹ Peridotite rock comprises most of Earth’s upper mantle. According to the NASA Exoplanets Archive (8/2015), 66 planets have substellar temperature $T_{ss} > 1673$ K and $r < 1.6 r_{\oplus}$ (Rogers 2015), and 103 planets have $T_{ss} > 1673$ K (assuming albedo = 0.1) and $r < 2.5 r_{\oplus}$ (Dumusque et al. 2014). Hot planets with masses and radii in the rocky-planet range include CoRoT-7b, Kepler-10b, Kepler-78b, Kepler-97b, Kepler-99b, Kepler-102b, Kepler-131c, Kepler-406b, Kepler-406c, and WASP-47e, with Kepler-36b and Kepler-93b slightly cooler than 1673K (Léger et al. 2009; Batalha et al. 2011; Hatzes et al. 2011; Weiss & Marcy 2014; Moutou et al. 2013; Carter et al. 2012; Pepe et al. 2013; Howard et al. 2013; Dai et al. 2015).

Pa (Fig. 2). In the second (compositionally buffered) case, Na, K, and Fe are replenished by surface-interior exchange; the exosphere fills with Na and K; and surface compositional evolution is very slow, because it is buffered by the massive reservoir of the planet’s interior. Surface composition will affect atmospheric abundances of Na and K (Wyttenbach et al. 2015; Nikolov et al. 2014; Heng et al. 2015), the properties of dust plumes streaming from disintegrating rocky planets (Budaj et al. 2015; Schlawin et al. 2016; van Lieshout et al. 2014), phase curves (Demory et al. 2016a), the potential for time-variability (Demory et al. 2016b), and reflectance/emission spectra (Hu et al. 2012; Samuel et al. 2014; Ito et al. 2015).

To what extent does fractional evaporation drive surface composition? To answer this question, we quantify the key controls on magma pool surface composition (Fig. 1). In this paper, we show that because atmospheric mass flux scales with vapor pressure and has a (super-)exponential dependence on temperature, winds are more important on the hottest planets than sluggish magma currents. Magma currents are paced by diffusion and relatively insensitive to pool temperature. This means that wind transport on the hottest planets permits compositionally-variegated pool surfaces (Fig. 3). However, winds are unimportant on relatively cool magma planets, so cooler magma pools are well-stirred (Fig. 3). The buoyancy evolution of melt pools undergoing fractional evaporation is the crucial second control: depending on initial composition, fractional evaporation can promote stratification or it can promote overturn. Together, these controls determine whether hot rocky exoplanet surfaces develop compositionally-evolved surfaces, or are repeatedly reset to bulk silicate composition.

Figs. 7 - 9 sum up what we found. §2 describes a minimal model of evaporation (winds) and circulation (currents). §3 describes how the pool’s composition evolves. We find two pathways that *might* permit a chemically-evolved surface composition: formation of a buoyant boundary layer within the pool, or evolution of the whole-pool composition toward a buoyant lag (Fig. 3). In §4.1 we discuss model assumptions and limitations. We discuss links to the solid mantle in §4.2, links to planet formation theory in §4.3, and planet disintegration in §4.4. We discuss links to observations in §5 and conclude in §6. Parameters and variables are listed in Table 1.

1.1. This Paper in Context.

Our focus is the chemical evolution of the surface. To get physical insights into chemical evolution, we use a simple model and make idealizations. We use simple models of the winds and currents. We do not resolve the details of atmosphere-ocean coupling. Instead, we emphasize how the winds and currents interact with the chemical evolution of the surface.

Following Léger et al. (2011), we view a thin, hemispheric melt pool as the conduit between the solid interior and the atmosphere (Fig. 1). We go beyond Léger et al. (2011) by considering horizontal convection in the magma pool, calculating the winds driven by vapor-pressure gradients, and – most importantly – considering the effects of fractional evaporation on residual-melt density. Because of these differences, we find that

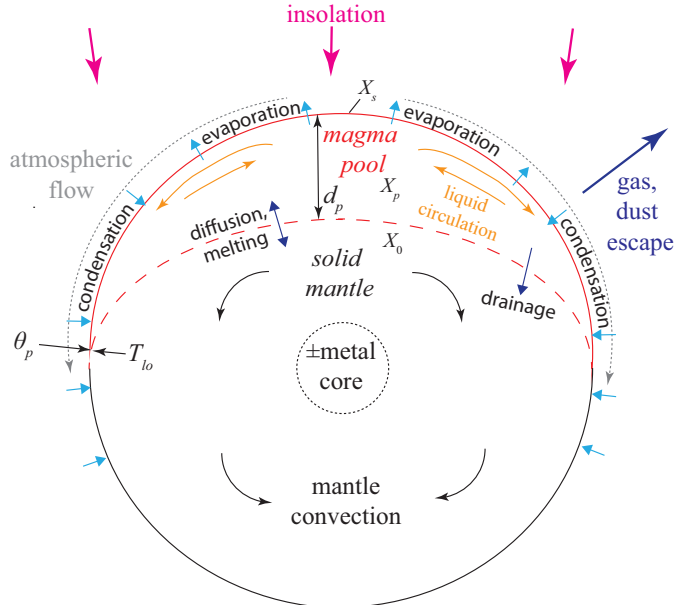


FIG. 1.— Processes shaping the surface composition of a hot rocky exoplanet. A magma pool of depth d_p and mean composition X_p (surface composition X_s) overlies a solid mantle of composition X_0 . Pool depth (d_p) is shown greatly exaggerated. T_{lo} corresponds to the temperature at the melt-pool’s edge. θ_p corresponds to the angular radius of the melt pool.

dynamic, compositionally-primitive surfaces are likely – in contrast to Léger et al. (2011), who conclude that melt pools should have compositionally-evolved, CaO-Al₂O₃ surfaces. Our approach to winds is anticipated by Castan & Menou (2011), who consider winds in a pure-Na atmosphere on a hot rocky exoplanet and show that winds have little effect on surface temperature. We approximate the solid silicate interior of hot super-Earths as isentropic, consistent with mantle convection models (e.g., van Summeren et al. 2011) which show that solid-state convection can even out large inter-hemispheric contrasts in interior temperature. To predict silicate-atmosphere compositions, we use the MAGMA code (Fegley & Cameron 1987; Schaefer & Fegley 2004, 2009, 2010; Schaefer et al. 2012) (Fig. 2). We assume negligible H₂O in the silicates.

Because magma planets are at close orbital distance, they are – and will remain – intrinsically easier to detect and to characterize than true Earth analogs. Already, phase curves, albedo constraints, and time-variability have been reported (Rouan et al. 2011; Demory 2014; Sheets & Deming 2014; Rappaport et al. 2012; Sanchis-Ojeda et al. 2015; Dragomir et al. 2014; Rappaport et al. 2014; Vanderburg et al. 2015; Demory et al. 2016a, Demory et al. 2016b). There is now a pressing need for self-consistent theory relating magma planet geophysics to data.

2. SETTING THE SCENE: CURRENTS VERSUS WINDS.

Magma pool surface composition, X_s , is regulated by magma currents (§2.2), silicate-vapor winds (§2.3), and the development of compositionally distinct surface zones (§2.4). If currents transport much more mass than winds, then X_s will be the same as pool-averaged composition X_p . However, X_s and X_p may differ if winds outpace

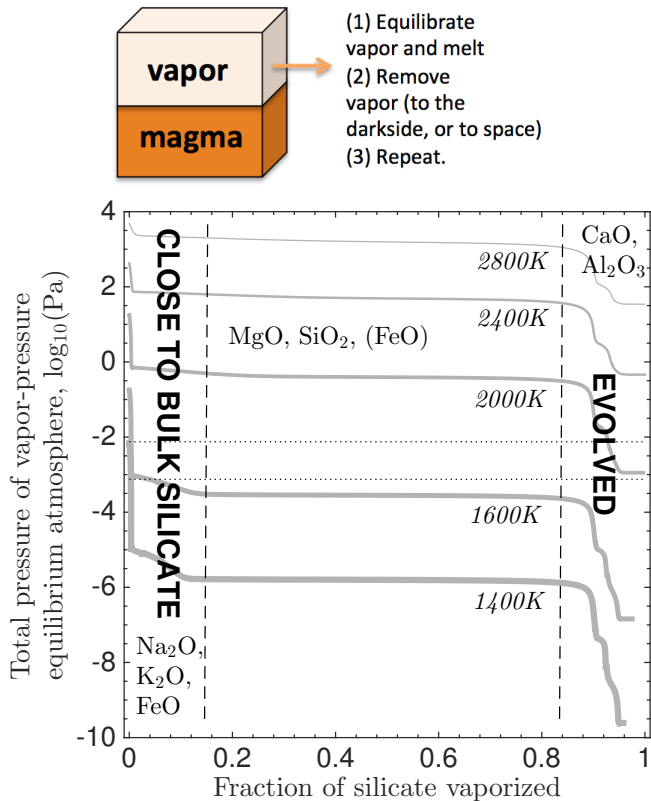


FIG. 2.— Trans-atmospheric distillation. *Top panel:* Sketch of fractional vaporization. *Bottom panel:* Decay of equilibrium vapor pressure during fractional vaporization of an initial composition corresponding to Bulk Silicate Earth (Table 2). Gray solid lines show fractional vaporization at different temperatures. Vertical dashed lines separate regions where different oxides control the density-evolution of the surface. Horizontal dotted lines show the pressure below which UV-driven escape is less efficient: optical depth = 1, assuming molar mass 30 g and photoabsorption cross-section of $10^{-22} \text{ m}^2 \text{ molecule}^{-1}$ (Reilman & Manson 1979), for surface gravities of 1.5 m s^{-2} (lower line), and 15 m s^{-2} (upper line).

currents (Fig. 3). X_p may be reset by drainage into the solid mantle (§2.5).

Liquid peridotite is not much more viscous than liquid water (Dingwell et al. 2004), and the almost-inviscid pool is subject to an insolation gradient (from center to edge). Circulation forced by a surface buoyancy gradient is remarkably slow (Sandström 1908; Stommel 1961; Wunsch 2005; Hughes & Griffiths 2008). This slow stirring can allow time for X_s to diverge from X_p , despite the low fractionation rate implied by the thin air (Fig. 2).

2.1. Melt Pools are Wide and Shallow.

We assume that the melt pool’s extent is set by a transition between fluid-like and solid-like behavior at a critical crystal fraction. Crystallizing magma acquires strength when increasing crystal fraction allows force to be transmitted through continuous crystal chains – “lock-up.” Lock-up occurs at a melt fraction of $\sim 40\%$ (Solomatov 2015). 40% melt fractions are reached at a lock-up temperature $T_{lo} \approx 1673\text{K}$ (Katz et al. 2003) (for a peridotitic composition; Appendix A). At T_{lo} , viscosity increases $>10^{10}$ -fold. Because of this large viscosity contrast, we

treat material inside the pool as liquid, and refer to material colder than T_{lo} as “solid.”

The pool angular radius, θ_p , is (in radiative equilibrium):

$$\theta_p \approx \cos^{-1} \left(\frac{T_{lo}}{T_{ss}} \right)^4 \quad (1)$$

where $T_{ss} = T_*(1-\alpha)^{1/4} \sqrt{r_*/2a}(4^{1/4})$ is substellar temperature, and the pool is centered on the substellar point.² Here, a is the semimajor axis, T_* is the star temperature, r_* is the star radius, and we assume basalt-like albedo $\alpha = 0.1$. (The optical albedo of liquid basalt is unknown, but we assume it to be similar to the albedo of solid basalt). Eqn. (1) applies if flow in the pool is sluggish, the atmosphere is optically thin, and atmospheric heat transport is negligible (Léger et al. 2011; Castan & Menou 2011) – all good assumptions (§2.2, §2.3). Most planets with magma pools have $\theta_p > 60^\circ$.

Crystal fraction increases with depth. This is partly because pressure favors crystallization (Sleep 2007). Also, temperatures deep in the planet’s solid mantle are smoothed-out by convective heat transport to the night side, so that the mantle below the pool has lower entropy than the pool (van Summeren et al. 2011). These effects give a pool-depth estimate $d_p \sim O(10) \text{ km}$ (Appendix B). Pool depth is further reduced by within-pool circulation (§2.2). Typically the melt pool is a shallow, hemispheric, magma ocean.

2.2. Magma Currents Refrigerate the Pool Interior, But Are Too Slow to Perturb Surface Temperature.

Magma flow is driven by gradients in T , X , or crystal fraction (Fig. 3). An estimate of magma speed (v_p) in the near-surface of the pool can be obtained by neglecting viscosity and inertia (this will be justified a posteriori). Then, balancing the pressure-gradient and rotational forces (geostrophic balance) yields

$$v_p \sim \frac{\nabla P}{f \rho_l} \quad (2)$$

where $\nabla P = g' \rho_l \delta_T / L = g_{pl} \Delta \rho_l \delta_T / L$, with $g' = g_{pl} \Delta \rho_l / \rho$ is the reduced gravity, g_{pl} is planet surface gravity, $\Delta \rho_l$ is the density contrast across the fluid interface at the bottom of the density boundary layer, $f \approx 2\Omega \sin(\theta_p/2)$ is the Coriolis parameter evaluated at $\theta_p/2$ (halfway between the substellar point and the latitudinal limits of the pool); here $\Omega = 2\pi/p$, with p the planetary period), δ_T is the thickness of the density boundary layer (where the density contrast can be due to T , X , or crystal fraction), and $L = \theta_p r$ is pool center-to-edge distance measured along the planet’s surface (planet radius is r). This model ignores currents at the equator, which are not directly affected by Coriolis deflection.

Consider flow driven by ∇T . Substellar radiative equilibrium temperatures can exceed T_{lo} by $>10^3 \text{ K}$.

² Eqn. (1) assumes a point source of light, but the host star fills $\sim 1 \text{ sr}$. Therefore, Eqn. (1) is used only for $\theta_p < \frac{1}{2}(\pi - \zeta)$, where ζ is the width ($^\circ$) of the twilight zone. To find θ_p for $\theta_p > \frac{1}{2}(\pi - \zeta)$, we linearly interpolate the stellar flux between limits of $\frac{1}{2}(\pi - \zeta)$ and $\frac{1}{2}(\pi + \zeta)$. This crude approximation sets Kepler 10b’s pool to cover 61% of the planet’s surface, which is reasonable.

TABLE 1
SELECTED PARAMETERS AND VARIABLES.

Parameter	Description	Value/units	Source/rationale
c_p	Heat capacity, atmosphere	850 J kg ⁻¹ K ⁻¹	
$c_{p,l}$	Heat capacity, magma	10 ³ J kg ⁻¹ K ⁻¹	
R	Gas constant	8.314 J K ⁻¹ mol ⁻¹	
H	Scale height, atmosphere	50 km	
l_v	Latent heat of vaporization, magma	6 × 10 ⁶ J kg ⁻¹	(1)
T_{AS}	Temperature, antistellar hemisphere	50 K	(2)
T_{lo}	Temperature at rheological transition (“lock-up”)	1673 K	(3)
α	Albedo (planet surface)	0.1	
γ	Evaporation coefficient (in Hertz-Knudsen equation)	0.2	(4)
$\delta\rho_l$	Density contrast (solid vs. liquid)	250 kg m ⁻³	
η_m	Viscosity, mantle	10 ¹⁸ m ² s ⁻¹	(5)
	Viscosity, magma	≲ 10 ² m ² s ⁻¹	(6)
κ	Diffusivity, thermocline	10 ⁻⁶ - 10 ⁻⁵ m ² s ⁻¹	Appendix C
κ_S	Mass diffusivity, sub- T_{lo} mantle	10 ⁻¹⁴ m ² s ⁻¹	(7)
κ_T	Thermal diffusivity, magma	5 × 10 ⁻⁷ m ² s ⁻¹	(8)
κ_X	Mass diffusivity, magma	10 ⁻⁹ - 10 ⁻¹⁰ m ² s ⁻¹	Appendix A
μ	Molar mass, atmosphere	34.15 g	(9)
μ_l	Molar mass, magma	100 g	
ρ_l	Density, magma	2500 kg m ⁻³	
ω	Fractional drainage (e.g., diapir pinch-off fraction)	0.3	
d_p	Depth of pool	m	–
E	Evaporation flux	kg m ⁻² s ⁻¹	
f	Coriolis parameter		
g'	Reduced gravity	m s ⁻²	
P, P_{ss}	Atmospheric pressure; pressure at substellar point	K	
r	planet radius	m	
\bar{T}, T_s, T_{ss}	Pool-average temperature; surface temperature; temperature at substellar point	K	
v	Speed of wind	m s ⁻¹	
v_p	Speed of magma overturning circulation in the near-surface of the pool	m s ⁻¹	
w	Speed of upwelling in melt pool	m s ⁻¹	
X_s, X_p, X_0	Compositions of melt-pool surface; pool; and solid silicate interior		
δ_T, δ_X	Thickness of thermal boundary layer; of compositional boundary layer	m	
Ω	Planet rotation rate	s ⁻¹	
θ_p, θ_0	Angular radius of pool; angular radius of evaporation-condensation boundary	deg	
ρ_0, ρ_δ	Density of silicate interior; density of chemical boundary layer	kg m ⁻³	
ρ_h	Maximum density during fractionation	kg m ⁻³	
ζ	Angular width of the twilight zone	deg	

REFERENCES. — (1) Öpik (1958). (2) Léger et al. (2011); they have “50-75 K”. (3) Katz et al. (2003). (4) Tsuchiyama et al. (1999); Grossman et al. (2000); Alexander (2001); Richter et al. (2002); Laretta et al. (2006); Fedkin et al. (2006); Richter et al. (2007, 2011). (5) Zahnle et al. (2015); Solomatov (2015). (6) Dingwell et al. (2004); Russell et al. (2003); Giordano et al. (2008); Zahnle et al. (2015); Solomatov (2015). (7) Brady & Cherniak (2010); Chakraborty (2010); Van Orman & Crispin (2010). (8) Ni et al. (2015). (9) Mean of μ_{SiO} and μ_{Mg} ; SiO and Mg dominate at intermediate stages of fractionation.

Magma expansivity is $\sim 10^{-4}$ K⁻¹ (Ghiorso & Kress 2004), so $\Delta\rho_l/\rho_l \sim 10\%$. The pool thermal boundary layer grows diffusively for as long as magma takes to move from the substellar point to the pool edge. Therefore $\delta_T \approx \sqrt{\kappa_T L / \Xi v_p}$, where κ_T is the diffusivity of heat (which we take to be the molecular thermal diffusivity, 5×10^{-7} m² s⁻¹; Ni et al. (2015)), and Ξ (“ageostrophic flow fraction”) is the scalar product of the magma-velocity unit vector and a unit vector that is directed from the center to edge of the pool. Now we can replace ∇P with $g' \rho_l L^{-1} \sqrt{\kappa_T L / \Xi v_p}$ and solve for thermal-flow timescale τ_T :

$$\tau_T \approx \frac{L}{\Xi v_p} \approx \kappa^{-1/3} \left(\frac{L^2 f}{\Xi g'} \right)^{2/3} \quad (3)$$

not counting any wind-driven circulation. A more sophisticated scaling (Vallis 2006) – including the variation of f

with θ , which is appropriate for meridional flow – yields

$$\tau_T \approx \kappa^{-1/3} \left(\frac{f^2 L}{\beta g'} \right)^{2/3} \quad (4)$$

$$\tau_T \approx 15 \text{ yr} \left(\frac{\kappa}{10^{-6} \text{ m}^2 \text{ s}^{-1}} \right)^{-1/3} \left(\frac{r}{r_\oplus} \right)^{1/4} \left(\frac{\theta_p}{\pi/2} \right)^{1.3} \left(\frac{1 \text{ day}}{p} \right)^{2/3} \quad (5)$$

where $\beta = (2\pi/pr) \cos(\theta_p/2)$, i.e. evaluated at $\theta = \frac{1}{2}\theta_p$. $\kappa = 10^{-4}$ m² s⁻¹ is possible with magma-wave breaking, but waves are likely small (Appendix C). Eqn. (5) is equal to Eqn. (3) with $\Xi = L\beta/f$. Eqns. (3) and (5) yield the same results within 21% for Kepler’s hot rocky exoplanets and $\Xi \sim 1$; we use the results of Eqn. (5).

Magma current speed in the surface branch of the overturning circulation is $v_p \sim L/\tau_T \sim 0.02$ m s⁻¹. The ratio of inertial to rotational forces (Rossby number

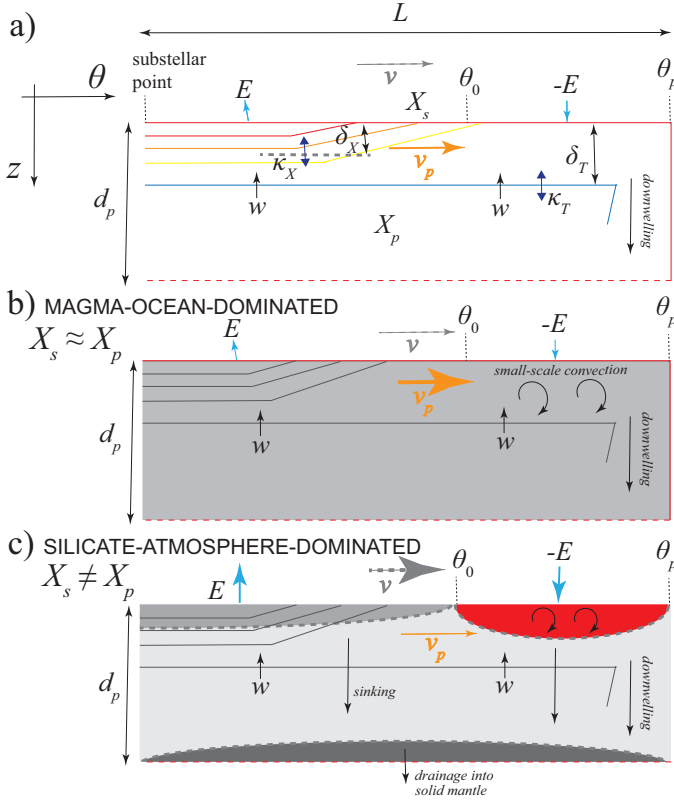


FIG. 3.— Magma pool internal structure. (a) Notation for the pool and boundary layer: d_p , pool depth; E , evaporation mass flux, v , wind speed; θ_0 , switch from evaporation to condensation; θ_p , pool edge; w , upwelling velocity; κ_T , magma thermal diffusivity; δ_T , thickness of thermal boundary layer (thermocline depth); v_p , net speed of the current corresponding to the surface branch of the overturning circulation; κ_X , magma compositional diffusivity; δ_X , thickness of compositional boundary layer. Downwelling occurs near the pool edge. Before downwelling, the thermal boundary layer is internally well-mixed by small-scale convection. (b) The ocean-circulation-dominated limit (uniform pool-surface composition). (c) The atmospheric-transport-dominated limit (variegated pool-surface composition). Pool-base material can redissolve, or drain into the solid mantle. In (b) and (c), red = more volatile than planet bulk-silicate composition, white = same volatility as initial planet bulk-silicate composition, gray = less volatile than initial planet bulk-silicate composition.

$Ro \equiv v_p/Lf \approx 10^{-3}$) and the ratio of viscous to rotational forces (Ekman number $Ek \equiv \mu/\Omega d_p^2 \ll 1$, where μ is kinematic viscosity) both turn out to be small, so our neglect of inertia and viscosity in Eqn. 2 is justified a posteriori.

Magma pool heat transport F_o (column W m^{-2}) is small. F_o is given by the product of v_p and the θ -gradient in boundary-layer column thermal energy,

$$F_o \approx \frac{\delta_T}{T_T} c_{p,l} \rho_m (T_{ss} - T_{lo}) \quad (6)$$

where $c_{p,l}$ is melt heat capacity ($10^3 \text{ J kg}^{-1} \text{ K}^{-1}$) and ρ_l is melt density (2500 kg m^{-3}), giving

$$F_o \approx 30 \text{ Wm}^{-2} \left(\frac{T_{ss} - 2000\text{K}}{T_{ss} - T_{lo}} \right), \quad (7)$$

$10^4 \times$ less than insolation (Fig. 9). F_o is also small

for pools with gradients in crystal fraction and in X . This is because the $\Delta\rho$ for freezing, for compositional differences, and for temperature gradients are all $O(10\%)$, and combining all three effects (\sim tripling g') only decreases the overturn time by half (Eqn. 5). Including the enthalpy of crystallization in Eqn. 6 would not alter this conclusion. Magma oceans are much less efficient at evening-out temperatures than are liquid-water oceans. This is because, for hot planets, radiative re-equilibration (scaling as T^4) defeats advection (which scales as T^1) (Showman et al. 2010). Because F_o is small, heat transport by melt-pool meridional overturning circulation cannot affect orbital phase curves (Hu et al. 2015). Furthermore, an initially global surface magma pool cannot be sustained by melt-pool overturning circulation: instead, global-surface magma pools beneath thin atmospheres will rapidly shrink to regional pools. Small F_o implies that ocean surface elevation smoothly tapers to near-zero at θ_p - so that levees of frozen, overspilt magma (Gelman et al. 2011) are not tall.

The thermal structure set up by horizontal convection (Fig. 3; Rossby 1965; Hughes & Griffiths 2008) consists of a cool deep layer at nearly-constant potential temperature, fed by narrow downwellings near the pool edge, and topped by a thin thermal boundary layer of thickness δ_T :

$$\delta_T \approx \kappa^{1/3} \left(\frac{f^2 L}{\beta g'} \right)^{1/3} \quad (8)$$

$$\delta_T \approx 15 \text{ m} \left(\frac{\kappa}{10^{-6}} \right)^{1/3} \left(\frac{r}{r_\oplus} \right)^{\sim 1/8} \left(\frac{\theta_p}{\pi/2} \right)^{2/3} \left(\frac{1 \text{ day}}{p} \right)^{1/3} \quad (9)$$

Downwellings ventilate the subsurface interior of the pool with material that has been chilled near the pool edge to $\approx T_{lo}$. Because the material just below δ_T has $T \approx T_{lo}$, d_p will not be much greater than δ_T . We assume $d_p = 10 \delta_T$; $d_p = 3 \delta_T$ is possible. Either option gives a pool depth that is $>100\times$ shallower than in the absence of overturning circulation (Eqn. B1) (Léger et al. 2011).

2.3. Atmospheric Redistribution of Mass Within the Pool Outpaces Atmospheric Removal of Mass From the Pool.

In this subsection we show that

- Atmospheric pressure P adjusts to the pressure in equilibrium with *local* surface temperature,
- Atmospheric transport is $\propto \partial P/\partial\theta$,
- Atmospheric energy and mass transport falls rapidly near the pool edge.

Busy readers may skip the remainder of this subsection.

Silicate atmospheres for $T_{ss} < 3000 \text{ K}$ (corresponding to all *Kepler's* planets) are thin enough to be in vapor-equilibrium (Wordsworth 2015; Heng & Kopparla 2012). Tenuous vapor-equilibrium atmospheres consisting of a single component equilibrate with *local* surface temperature on horizontal distances of ~ 10 atmospheric scale heights $H = RT/\mu g \approx (8.3 \text{ J mol}^{-1} \text{ K}^{-1} \times 2400\text{K}) / (\sim 0.03 \text{ kg mol}^{-1} \times 15 \text{ m s}^{-2})$

≈ 50 km for hot-rocky-exoplanet silicate atmospheres, where R is the gas constant, μ is molar mass, and g is planet surface gravity (Ingersoll 1989; Castan & Menou 2011). The appropriateness of the single-component assumption is discussed in §4.1. μ is set to the mean of μ_{SiO} and μ_{Mg} ; SiO and Mg dominate at intermediate stages of fractionation (Schaefer & Fegley 2009). Because $H \ll$ planet radius (r), the approximation that pressure P adjusts to surface temperature T_s locally is well-justified. With local adjustment, pressure gradients are everywhere directed away from the substellar point. Because T_s is low on the nightside, nightside pressures are close to zero. Because the dayside atmosphere expands into near-vacuum on the nightside, wind speeds are $v \sim \sqrt{RT/\mu} \sim 1$ km s $^{-1}$ (sound speed), where T ($\sim \bar{T}$) is the hot-zone atmospheric temperature. At least for the analogous case of Io, surface friction is ineffective in braking the flow (Ingersoll et al. 1985). Inertial forces modestly exceed rotational forces ($v/Lf \approx 4$ for $p = 3$ days), so winds are also directed away from the substellar point. Winds transport mass from an evaporation region near the substellar point to cold-traps. Because cold-traps are outside the pool, loss of mass from the pool requires atmospheric flow past θ_p . Therefore the temperature at θ_p regulates loss from the pool (given the approximation of local adjustment) – this temperature is T_{lo} . At T_{lo} , the pressure P_{eq} in equilibrium with silicate after 20 wt% fractional evaporation from an initial composition of Bulk Silicate Earth is 1×10^{-2} Pa ($\sim 5 \times 10^{-4}$ kg m $^{-2}$ for Super-Earths; Schaefer & Fegley 2009). The flux over the pool perimeter is thus $m_f = vP_{eq}/g \sim 0.5$ kg s $^{-1}$ m $^{-1}$. For hemispheric pools, this corresponds to a column loss rate of $m_f/\rho_l r \sim 5 \times 10^{-4}$ m yr $^{-1}$ averaged throughout the pool ($\rho_l \approx 2500$ kg m $^{-3}$, $r \sim 10^7$ m). So the time for the pool to be depleted of the constituent that is dominant in the vapor is

$$\tau_d \sim \frac{d_r g r f_c \rho_l}{v P_{eq}(X_s, T_{lo})} \quad (10)$$

$$\approx 2 \times 10^5 \text{ yr} \left(\frac{P_{eq}(\text{B.S.E.}@20\%, T_{lo})}{P_{eq}(X_s, T)} \right) \left(\frac{d_r}{100 \text{ m}} \right) \left(\frac{f_c f_g}{1} \right) \quad (11)$$

where d_r is the effective depth of mixing (i.e the column depth of melt that can be obtained by depressurization and melting on timescale τ_d), f_g is a geometric correction equal to 1 if the pool only samples material vertically beneath it, and f_c is the mass-fraction of the component in the magma.

τ_d falls as T rises, because P_{eq} (and thus mass flux) increases super-exponentially with T . $P_{eq}(T)$ (for an initial composition of Bulk Silicate Earth, $1400\text{K} < T < 2800\text{K}$), is well-fit by

$$\log_{10}(P_{eq}) \approx k_1 \exp(k_2 T_s) \quad (12)$$

where $k_1 = \{-34.7, -60.1, -60.2\}$ and $k_2 = \{-0.00112, -0.00122, -0.00101\}$ for small (<0.01), intermediate (0.5) and large (>0.9) fraction of silicate vaporization, respectively, and P_{eq} is in bars (Fig. 2). Pool mean surface temperatures \bar{T} are typically

500K higher than pool-edge temperature T_{lo} . Column-integrated atmospheric mass flux scales with the gradient in the pressure and with the surface pressure. Because the surface pressure increases exponentially with local temperature, atmospheric transport near the center of the pool is much faster than atmospheric transport over the edge of the pool. For example, for CoRoT-7b, a basic calculation shows (Fig. 7) that the trans-atmospheric transport over the evaporation-condensation boundary within the pool is 10^3 kg s $^{-1}$ (m perimeter) $^{-1}$, which is $5000\times$ greater than transport over the edge of the pool. Therefore the pool can internally differentiate – develop compositional boundary layers – faster than pool material can be lost by atmospheric flow over the edge of the pool. This justifies our quasi-steady-state approximation for mass exchange within the pool.

In addition to the strong T dependence, τ_d is sensitive to X_s . As fractional evaporation progressively removes the more volatile components, P_{eq} falls (Fig. 2).

τ_d is proportional to d_r . d_r can vary from less than pool thermocline depth δ_T (10m) up to planet radius r (10^7 m). Although as little as 10^8 yr are required to remove Na from an Earthlike planet ($f_g = 2$; $d_r \approx 10^7$ m; $f_c \sim 0.0035$, Table 2), 4×10^{10} yr are required for full planet evaporation ($f_g = 2$; $d_r \approx 10^7$ m; $f_c \sim 1$).

Atmospheric heat flux (W m $^{-2}$) is given by

$$F_a \approx l_v P \left(\frac{v}{gL} \right) \approx l_v k_1 \exp(k_2 T_s) \left(\frac{v}{gL} \right) \quad (13)$$

$$F_a \approx 60 \text{ W m}^{-2} \left(\frac{P(T_s)}{1 \text{ Pa}} \right) \left(\frac{R_{\oplus}}{R} \right)^{\sim 3/2} \quad (14)$$

where $l_v = 6 \times 10^6$ J kg $^{-1}$ is magma's vaporization enthalpy (neglecting sensible heat transport and wind kinetic energy, which are both $<10\%$ of l_v). F_a equals absorbed insolation at 3500 K. For $T \ll 3500$ K, F_a is small compared to insolation (Castan & Menou 2011).

Loss of mass to cold traps is supplemented by escape to space. Atmospheric escape is 10^8 kg s $^{-1}$ for a planet around a 1 Gyr-old Sun-like star – if escape is EUV-flux-limited and 100% efficient (Valencia et al. 2010). Efficiencies for rocky planets are poorly constrained (Murray-Clay et al. 2009; Owen & Alvarez 2015; Tian 2015; Ehrenreich et al. 2015). Even at 100% efficiency, escape to space corresponds to a hemisphere-averaged vertical breeze of 10 m s $^{-1}$ (4×10^{-3} m/yr of melt-column ablation); this does not greatly alter the conclusion that $P \approx P_{eq}$, and so liquid remains stable (Ozawa & Naga-hara 1997). Hydrostatic Roche-lobe overflow is minor for Super-Earths (Rappaport et al. 2013). Summing escape-to-space and loss to cold traps, Earth-sized planets cannot be wholly processed in the age of the Universe, but smaller planets can disintegrate (§4.4).

2.4. Competition Between Evaporation & Circulation Affects Magma Pool Surface Composition

Surface composition for melt pools is set by competition between the pool's overturning circulation (which refreshes the surface on timescale τ_T , §2.2), and flow in the atmosphere, which produces a chemically differentiated boundary layer on a timescale τ_X . Consider a pool with two chemical components, volatile A and refractory

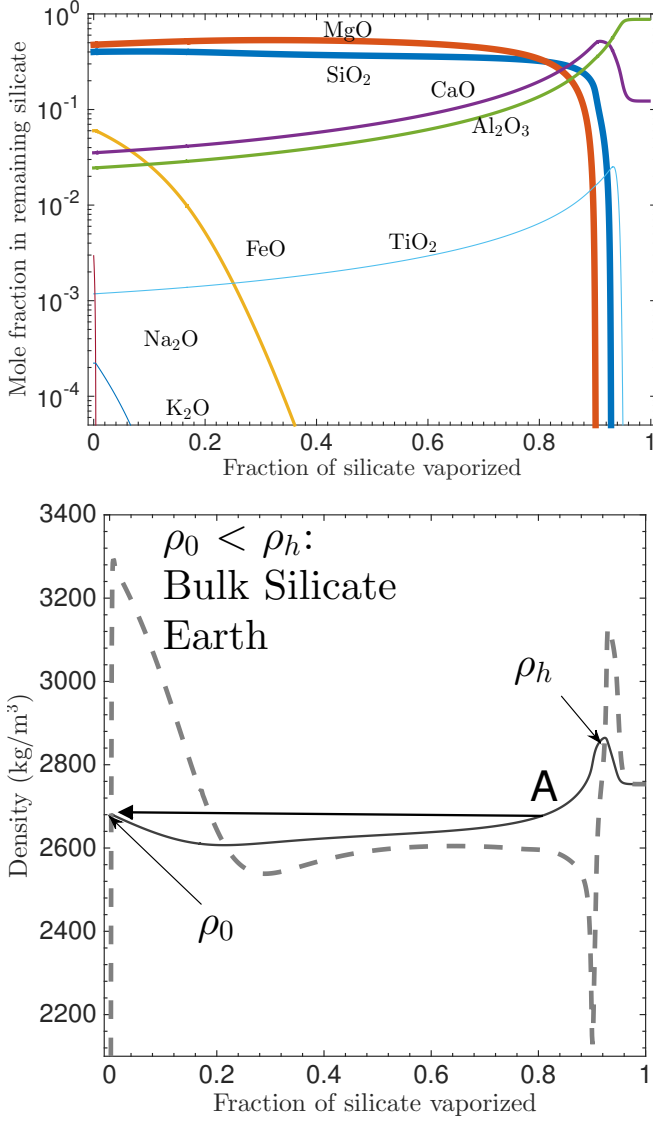


FIG. 4.— Fractional vaporization at 2000K of an initial composition corresponding to Bulk Silicate Earth. *Upper panel:* Residual magma compositional evolution. Na and K are lost rapidly. *Lower panel:* Density evolution. Thin black solid curve corresponds to the density of residual magma, and thick gray dashed curve corresponds to the density-upon-condensation of the gas. ρ_0 corresponds to un-fractionated magma density. ρ_h corresponds to the maximum density at >70 wt% fractional vaporization. At point A, the surface boundary layer sinks into the interior.

Z. ‘A’ evaporates from the surface preferentially near the substellar point, and condenses on the surface beyond the evaporation-condensation boundary – the angular distance (θ_0) where the sign of net evaporation changes. If $\rho_A > \rho_Z$, then the residual melt in the evaporation zone becomes buoyant, and the residual melt in the condensation zone will sink into the pool interior. If $\rho_A < \rho_Z$, then the residual melt in the condensation zone becomes buoyant, and the residual melt in the evaporation zone will be unstable to sinking. Therefore, regardless of whether A or Z is denser, the magma pool will (given time) acquire a variegated surface, with parts of the surface having evolved X_s and parts of the surface being close to the initial composition. (Here we assume that there is a large density difference, and that $\theta_p > \theta_0$.) Dif-

usive exchange with the deeper layers of the pool will initially resupply/remove constituents faster than fractional evaporation E , so the time to form a chemically variegated surface is set by diffusion-ablation balance

$$\tau_X \approx \left(\frac{\kappa_X}{E_e/\rho_l} \right) \left(\frac{\rho_l}{E_e} \right) = \kappa_X \left(\frac{\rho_l^2}{E_e^2} \right) \quad (15)$$

where κ_X is molecular diffusivity and $\overline{E_e}$ is the mass-loss rate due to fractional evaporation. The first term in brackets in Eqn. (15) is the compositional boundary layer thickness $\delta_X = \kappa_X \rho_l / \overline{E_e}$, and the second term in brackets is the compositional boundary-layer processing speed. κ_X is 10^{-9} - 10^{-10} m² s⁻¹ for liquid silicates at hot magma pool temperatures (Karki et al. 2010; de Koker & Stixrude 2011). The Lewis number (κ_X / κ_T) is < 0.01 . Increasing κ_X slows down chemical boundary layer development – because chemical diffusion refreshes the surface with fresh material. By contrast, increasing κ_T speeds up horizontal convection – because upwelling via thermal diffusion is needed to close the circulation (Eqn. 5).

When $\tau_X/\tau_T \ll 1$, chemical differentiation between the surface boundary layer and the interior of the magma pond may occur (Fig. 3c). If chemical fractionation occurs, then the atmosphere effectively samples the chemically-fractionated skin layer δ_X . By contrast, when $\tau_X/\tau_T \gg 1$, the atmosphere effectively samples a well-mixed pool (Fig. 3b).

$\tau_X/\tau_T \ll 1$ is neither necessary nor sufficient for a buoyant lag to form. If chemical-boundary-layer density ρ_δ exceeds the initial density ρ_0 , then the incompletely-differentiated skin layer can founder and be replaced at the surface by material of the starting composition. Alternatively, if chemical-boundary-layer density ρ_δ is less than the initial density ρ_0 , the *entire pool* might evolve into a (well-mixed) lag that is compositionally buoyant with respect to the mantle, even if $\tau_X/\tau_T \gg 1$.

2.5. Magma Pool Composition Cannot be Buffered by Molecular Diffusion, but Can be Reset by Drainage Into the Mantle.

Pool depth stays steady during evaporation. This is because melt-back of the stratified solid mantle at the base of the pool keeps pace with evaporative ablation of the pool surface.³

$$2.32\sqrt{\kappa_T\tau_d} \gg \frac{E}{\rho_m}\tau_d \quad (16)$$

Melt-back dilutes the fractionating pool with un-fractionated material, slowing compositional evolution. (We assume that any solid phases that form at the base of the pool by reactions between the liquid and the ascending solid rock, such as spinels, are swept up into the pool and remelt).

Using the atmospheric model (Appendix D) to compute E , we find that molecular diffusion within the solid mantle is too slow to delay whole-pool fractional evaporation:

$$\delta_p \gg 2.32\sqrt{\kappa_S\tau_d} \quad (17)$$

³ Latent heats of fusion are $<20\%$ l_v .

where κ_S ($\lesssim 10^{-14}$ m² s⁻¹) is a molecular diffusivity in crystalline silicates (Brady & Cherniak 2010).⁴

Suppose that the pool's composition is uniform and in steady state, and the pool is much less massive than the time-integrated mass lost to trans-atmospheric transport. Then, mass balance requires that the material lost from the pool must have the same composition as the melt-back input to the pool – i.e., bulk-silicate composition (Wang et al. 1994; Richter 2004; Ozawa & Nagahara 2001). The pool adjusts to a composition X_b (buffer) that satisfies this condition. Because of the wide range of volatilities for the component oxides (Fig. 2), X_b is CaO/Al₂O₃-dominated, with tiny proportions of Na₂O and K₂O, and a low total atmospheric pressure (steady, uniform, evolved surface composition) (Fig. 2).

If $\rho(X_b) < \rho(X_0)$, then $X_p = X_b$ is a steady state. However, if $\rho(X_b) > \rho(X_0)$, then the intrinsically dense material in the pool may be unstable to finite-amplitude perturbations in the pool-base. X_p can then be intermittently reset to X_0 by pool drainage into the mantle.

The pool can drain by infiltrating, by diking, or by forming one or more approximately spherical blobs (diapirs). Diapirism is rate-limited by the time needed to concentrate a hemispheric shell into a spherical diapir (Honda et al. 1993; Reese & Solomatov 2006). In numerical simulations (Honda et al. 1993), diapirs form on a timescale

$$\tau_f \approx \frac{27\eta_m}{8\pi\omega^{2/3}G\rho_0^2r^2} \left(\frac{\rho(X_b)}{\rho_0} - 1 \right)^{-1} \left(\frac{r^3}{(r-d_p)^3} - 1 \right)^{-2/3} \quad (18)$$

$$\tau_f \approx 50 \text{ Kyr} \left(\frac{\eta_m}{10^{18} \text{ Pa s}} \right) \quad (19)$$

where η_m is mantle viscosity ($\sim 10^{18}$ Pa s; Zahnle et al. (2015)), G is the gravitational constant, r is planet radius, and $\omega \approx 0.3$ is the fraction of the hemispheric shell's volume that contributes to the diapir. To obtain Eqn. (19), we assume $\rho(X_b)/\rho_0 \approx 1.1$. In order to drain, the diapir density must exceed the *solid* density, which might occur through compositional evolution, or through partial freezing by ventilation by cool currents at the base of the pool. $\tau_f \approx \tau_\kappa$ (Eqn. 16). Diapir volume will be $V_d = 2\pi\delta_p\omega r^2$ giving diapir radius $O(10^2)$ km. As the diapir sinks, a maximum of $V_d \rho_m \Delta \rho G M_{pl} / r \sim 10^{26}$ J of gravitational potential energy is converted to heat, enough to warm the planet's interior by 0.01 K per event – delayed differentiation (here, $\Delta\rho$ is the fractional contrast in density). Alternatively, melting of the adjacent mantle from viscous dissipation as the diapir sinks may entrain lighter fluid and halt the descent of the diapir. Although a single diapir is the most linearly-unstable mode (Ida et al. 1987, 1989), smaller diapirs (or dikes, or magma solitons) may be more realistic, reducing ω . As $\omega \rightarrow 0$, composition becomes steady. For $\omega \neq 0$, composition is unsteady.

⁴ Melt-pool depth (i.e., a few times greater than the δ_T given in Eqn. 9) is the relevant length scale for diffusion. An order-unity depletion (relative to original bulk-silicate composition) in the abundance of a chemical component in the pool can be replenished by drawdown of the same chemical component from a layer in the solid mantle that is δ_p -thick.

3. HOW MANTLE COMPOSITION REGULATES SURFACE-INTERIOR EXCHANGE: DENSITY EVOLUTION AND ITS IMPLICATIONS.

Evaporation-versus-circulation competition (§2) determines whether pool surface composition evolves in lock-step with whole-pool composition. In cooler magma pools, circulation defeats evaporation, and homogenizes pool composition. However, hotter magma pools will have compositionally-variegated surfaces. Compositionally-evolved portions of the surface may spread to form buoyant shroud layers, depending on initial composition. Dense basal layers will form, and may drain into the mantle.

Now, we use a melt-density model (Appendix A) to track the density of residual magma during fractional vaporization. Residual-magma density determines whether the fractionated reservoir is unstable to sinking (§3.1). To calculate evaporation rates, we use a 1D atmospheric model (Appendix D).

3.1. Initial Bulk-Silicate Composition X_0 Determines Magma-Pool Stability.

Rocky-planet destruction by evaporation has five steps: (1) loss of atmophiles (H, C, N, S, P, halogens, noble gases), oceans, and continents; (2) loss of Na+K, (3) loss of Fe+Mg+Si, (4) loss of the residual Al+Ca(+Ti); (5) loss of the metal core. We consider steps 2, 3, and 4, for a range of bulk silicate (mantle + crust) compositions (Table 2). The main density-determining components are SiO₂, CaO, Al₂O₃, MgO, FeO(T), Na₂O, and K₂O (Fig. 2). (FeO(T) can stand for FeO, Fe₂O₃, Fe₃O₄, or a mixture, depending on oxidation state). Cations are lost from the melt in the order Na > K > Fe > (Si, Mg) > Ca > Al.

Output from the **MAGMA** code for fractional evaporation of melt at 2000K (Bulk Silicate Earth composition) is shown in Fig. 4. Initially the magma outgasses a Na/K rich mix which (upon condensation) has a low density. The *residue* density does not change much at this stage because Na₂O and K₂O are minor components of the melt. Next to outgas is an Fe-rich mix. Upon condensation, this material is denser than the magma underlying it; the Fe-rich material will sink to the base of the pool. Continuing beyond ~ 22 wt% fractional evaporation, the density of the residual magma increases. This will lead to small-scale compositional convection within the evaporation-zone compositional boundary layer, but the boundary layer as a whole still has lower density than the initial density (ρ_0). The still-buoyant boundary layer continues to evolve to a more-fractionated composition (the gas is now dominated by Mg, Si, and O). Beyond 81 wt% fractional vaporization (point A in Fig. 4), the density of the now-well-mixed boundary layer exceeds ρ_0 . That is because the boundary layer is now CaO-rich (~ 20 % molar), and CaO is dense (Fig 12). We define ρ_h as the maximum density at >70 wt% fractionation. Beyond A, the boundary layer sinks into the underlying magma. Fractional evaporation beyond A is not possible.⁵ The surface reaches a dynamic steady state, with

⁵ To see that ρ_h is also a barrier for condensates beyond the evaporation-condensation boundary (θ_0), suppose that after some time the supply of fresh gas from the evaporation zone to the condensation zone is shut off. After shut-off, some gas will condense

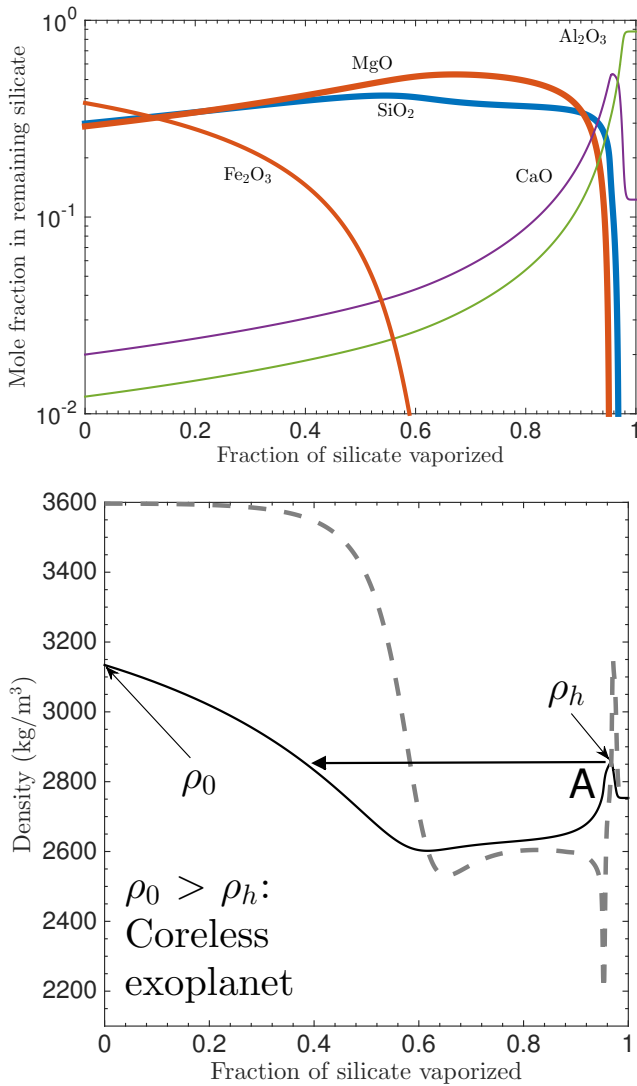


FIG. 5.— Fractional vaporization at 2000K of an initial composition corresponding to the Coreless Exoplanet of Elkins-Tanton & Seager (2008a). *Upper panel:* Residual-magma compositional evolution. *Lower panel:* Density evolution. Thin black solid curve corresponds to the density of residual magma, and thick gray dashed curve corresponds to the density-upon-condensation of the gas. ρ_0 corresponds to unfractionated magma density. ρ_h corresponds to the maximum density at >70 wt% fractional vaporization. At point A, small-scale convection within the surface boundary layer is maximal, but the boundary layer as a whole remains buoyant.

parts of the surface covered by fresh material, and parts of the surface covered by evolved material that is nearly ready to sink. Atmospheric pressure will not be much less than the pressure above an unfractionated melt. The relevant reservoir for long-term net pool compositional evolution is the entire silicate mantle (assuming dense material drains efficiently into the solid mantle).

Fractional vaporization of an FeO-rich exoplanet (Elkins-Tanton & Seager 2008a) proceeds differently (Fig. 5). At 0 wt% fractionation, the melt is $\sim 10\%$

on the solid planet and will fractionate towards an CaO-Al₂O₃ lag. For rocky planets with $\theta_p > \theta_0$ (~ 80 wt% of known hot rocky exoplanets), the dense FeO_x-rich residual liquids will sink to d_p . The lighter materials will float and so will evolve towards CaO-MgO-Al₂O₃-SiO₂ (CMAS) liquids, but because $\rho_h > \rho_0$ their boundary layers will be homogenized by small-scale convection and then sink.

TABLE 2
COMPOSITIONS INVESTIGATED (WT%)

	Bulk Silicate Mercury	Bulk Silicate Earth	Bulk Silicate Mars	Coreless Exoplanet
SiO ₂	47.10	45.97	45.0	28.8
MgO	33.70	36.66	30.6	18.7
Al ₂ O ₃	6.41	4.77	3.06	2.0
TiO ₂	0.33	0.18	0.14	—
FeO(T)^a	3.75	8.24	18.15	48.7
CaO	5.25	3.78	2.48	1.8
Na ₂ O	0.08	0.35	0.051	—
K ₂ O	0.02	0.04	0.03	—
Ca:Fe ^b	1.3	0.42	0.13	0.04
Source	(1)	(2)	(3)	(4)

REFERENCES. — (1) Morgan & Anders (1980); Zolotov et al. (2013); (2) Schaefer & Fogley (2009); (3) Dreibus & Wanke (1985); (4) Elkins-Tanton & Seager (2008a).

^a [FeO(T)] = [FeO], except for Coreless Exoplanet, for which [FeO(T)] = [Fe₂O₃].

^b Weight ratio of Ca to Fe, decreasing with semimajor axis in the solar system. Although [FeO]’s effect on stratification can be offset by high [CaO], Ca is refractory (Grossman & Larimer 1974) and so [FeO] and [CaO] are anti-correlated in rocky planets.

denser than the unfractionated melt of Bulk Silicate Earth. The FeO-rich pool will initially develop a stably-stratified layer due to loss of Fe. At 60 wt% fractionation, density starts to rise and small-scale convection develops within the boundary layer (Fig. 5). At 95 wt% fractionation, the extent of convection reaches its maximum - but convection is still confined within the boundary layer. The boundary layer stays buoyant; re-equilibration with the deep interior is inhibited. The relevant reservoir depth for fractionation is δ_X or δ_T for $\tau_T \gg \tau_X$, or the entire pool for $\tau_T \ll \tau_X$. $\tau_d(\delta_X)$, $\tau_d(\delta_T)$ and $\tau_d(\delta_p)$ are all $\ll 1$ Gyr (Eqn. 11). Therefore, FeO-rich planets are vulnerable to surface-composition evolution leading to an extremely low-pressure atmosphere (Fig. 2).

Vulnerability to stratification is proportional to $(\rho_0 - \rho_h)$. $(\rho_0 - \rho_h)$ is shown in Fig. 7 for a range of pool \bar{T} and mantle compositions (Table 2). High [FeO] makes stratification more likely, because FeO is both dense and volatile. When [FeO] is high, ρ_0 is high. For a high-[FeO] world, the near-complete loss of FeO before 70 wt% fractionation greatly decreases residual-magma density relative to ρ_0 . Therefore the Ca-driven “uptick” in density at high fractionation does not reach ρ_0 (Fig. 5). Therefore $(\rho_0 - \rho_h)$ is high (Fig. 7). If [FeO] is low, then stratification is impossible. If [FeO] is high, then stratification is possible.

To calculate the time τ_X required for compositional evolution (Fig. 8), we need to know the mean evaporation rate (\bar{E}) within the pool. To find \bar{E} , we use a 1D atmospheric model (Appendix D), which largely follows Castan & Menou (2011) and Ingersoll (1989). Typical 1D model output is shown in Fig. 6.

3.2. Summary of Model Output.

By combining Eqns. (5)-(11) and (D2)-(D5), we can predict the surface composition and atmospheric pressure for each magma planet. Predictions for specific magma planets are shown in Table 6. Figs. 7 - 9 show the expected steady-state outcomes:

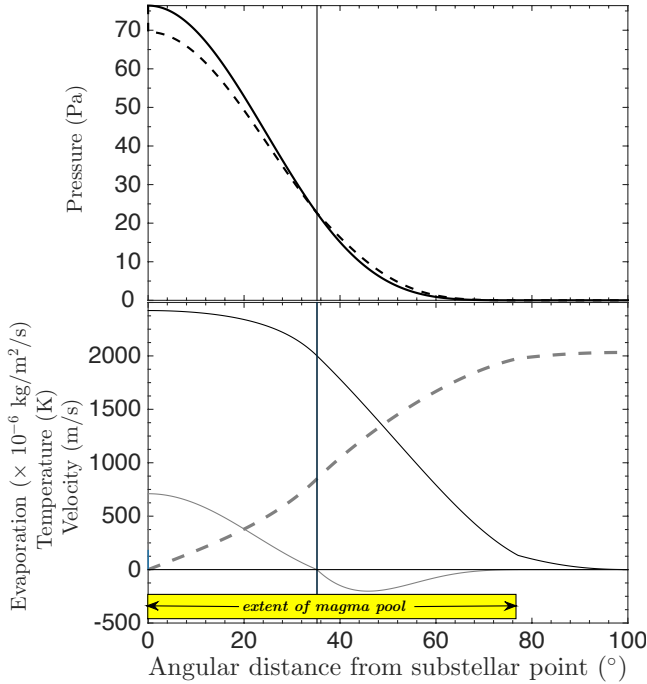


FIG. 6.— Example of atmospheric-model output (for CoRoT-7). *Top panel:* Thick black lines correspond to pressure (solid is uncorrected for evaporative flux, dashed is corrected for atmospheric flux). *Bottom panel:* Light gray line corresponds to evaporation (negative for condensation). Thin solid line corresponds to air temperature (K). Thin dotted line corresponds to wind speed (m s^{-1}). The magma pool extends from a region of moderately high pressure (75 Pa) to a region of very low pressure. Results are shown at 50 wt% fractionation, for an initial composition corresponding to Bulk Silicate Earth. (See Appendix D for details).

- If hot rocky exoplanets are FeO-rich, then pool compositions will be steady, uniform, and dominated by CaO and Al_2O_3 . We refer to this state as a “buoyant shroud.” Atmospheres will be $\lesssim O(1)$ Pa (Fig. 2). Venting of Na and K from the pool will be minor, and escape-to-space will be reduced.
- If hot rocky exoplanets are FeO-poor, then pool composition will be time-variable, and probably variegated. Averaged over timescales $> \tau_f$, atmospheres will be thick. Escape-to-space will not be limited by the supply of atmosphere (Fig. 2).
- τ_T increases as \bar{T} increases, because hotter pools are wider – with increased $L(\theta_p)$ and $f(\theta_p)$.

3.3. Stratification Should Occur for Mantles Formed From Oxidized Planetesimals.

[FeO(T)] measures the extent to which a planet’s building-blocks have been oxidized. (For this paper, $[\text{FeO(T)}] = [\text{FeO}]$ for the Bulk Silicate Earth composition, the Bulk Silicate Mercury composition, and the Bulk Silicate Mars composition, and $[\text{FeO(T)}] = [\text{Fe}_2\text{O}_3]$ for the Coreless Exoplanet composition.) The most likely oxidant is water.

FeO(T) is not expected from condensation-from-vapor of an solar-composition protoplanetary disk: fast conden-

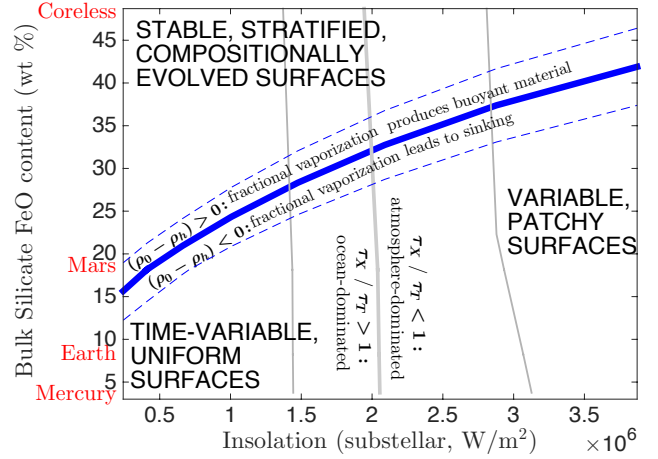
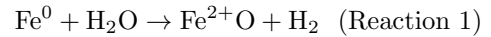
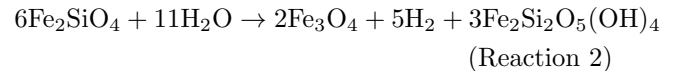


FIG. 7.— Magma planet phase diagram. Blue and gray lines divide the phase diagram into quadrants. Blue lines correspond to stratification index $(\rho_0 - \rho_h)$ contoured at $+50 \text{ kg m}^{-3}$ (top dashed blue line), 0 kg m^{-3} (thick solid blue line), and -50 kg m^{-3} (bottom dashed blue line), using Ghiorso & Kress (2004) equation-of-state. Planets **below the line** are **unlikely** to have $\text{CaO}/\text{Al}_2\text{O}_3$ -dominated surfaces, planets **above the line** are **likely** to have $\text{CaO}/\text{Al}_2\text{O}_3$ -dominated surfaces. Gray lines (near vertical) correspond to ocean-dominance index τ_X/τ_T , contoured at 10 (left thin solid line), 1 (thick line), and 0.1 (right thin solid line), for 50 wt% vaporization. The lower-left quadrant corresponds to ocean-dominated planets with uniform, but time-variable surfaces, driven by thermal overturn. The lower-right quadrant corresponds to atmosphere-dominated planets with time-variable and compositionally-variegated surfaces driven by evaporative overturn. The upper two quadrants correspond to planets with stable, stratified, $\text{CaO}-\text{Al}_2\text{O}_3$ -dominated surfaces (compositionally evolved). Calculations fix p (to 0.84 days), r (to $1.47 R_\oplus$), and g (to $1.9 g_\oplus$), appropriate for Kepler-10b. Named compositions (red) are from Table 2. Additional results are shown in Fig. 18.

sation of solar-composition gas at the snowline (145K–170K) forms large quantities of iron (Fe + FeS), Mg-silicates, and H_2O , but FeO(T) in silicates is not expected because of kinetic effects (Krot et al. 2000; Podolak & Zucker 2004; Lewis 2004; Moynier & Fogley 2015). However, FeO_x production occurs readily via metal-water reactions (Rosenberg et al. 2001; Lange & Ahrens 1984; Dreibus & Wanke 1987):



on planetesimals and larger bodies; as well as via water-rock reactions, such as (Früh-Green et al. 2004; McCollom & Bach 2009; Klein et al. 2013):



as well as by condensation of silicates from a water-enriched vapor, for example a plume produced by impact into an water-rich target planetesimal (Fedkin & Grossman 2016). FeO(T) produced by Reactions 1 and 2 remains in the silicate mantle. Because of accretion energy, growing planets get hotter. Above $\sim 900\text{K}$, Reaction 2 is thermodynamically unfavorable. However, iron oxidation can continue if accreted material includes both Fe-metal and H_2O (e.g., via Reaction 1) (Kuwahara & Sugita 2015). [FeO(T)] production is also favored by partitioning of metallic Fe into the core and by H-escape (Frost et al. 2008; Zahnle et al. 2013; Wade & Wood 2005).

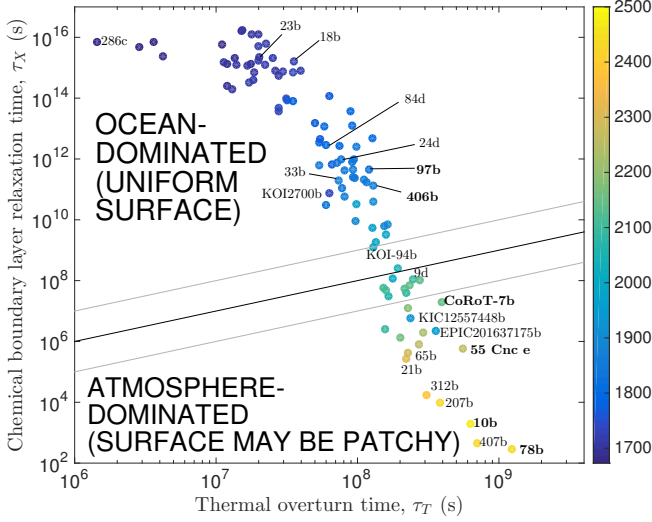


FIG. 8.— Pool-overturn timescales vs surface-fractionation timescales. Relatively-cool magma pools are “ocean-dominated” - stirred by currents more rapidly than boundary-layer chemical segregation can occur (Fig. 3b). Hotter magma pools are “atmosphere-dominated,” with compositionally-variegated surfaces (Fig. 3c). The black line corresponds to chemical fractionation time (τ_X) equal to pool-overturn time (τ_T). The gray lines show $10\times$ uncertainty. Color of dots corresponds to pool \bar{T} (K). τ_X decreases rapidly as planets get hotter. The slope of the shallow branch (small magma pools) is set by τ_T ’s control of θ_p ; for large magma pools, $\theta_p \sim 90^\circ$, and the slope of the steep branch is set by the effect of p on rotational forces (Eqn. 5). Selected planets are labeled; labels without prefixes are Kepler planet numbers. **Bold** highlights planets with measured densities. We exclude the putative planets orbiting KIC 05807616 (Krzesinski 2015). Results assume fractional vaporization of 20% of fractionating volume. Disintegrating rocky planets are assigned $r = 0.3 r_\oplus$, $M \approx 0.01 M_\oplus$.

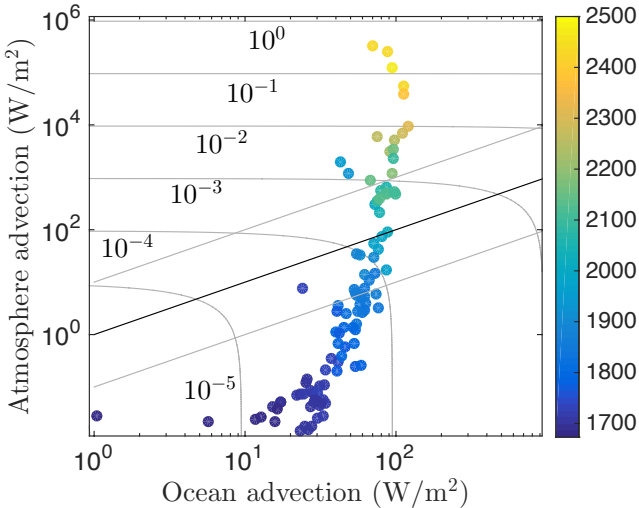


FIG. 9.— Atmospheric latent-heat transport compared to magma-current heat transport and to insolation. Color of dots corresponds to pool \bar{T} (K). Contours show the ratio of the total advected flux (currents + winds), divided by insolation for an “average” hot rocky exoplanet. Results assume fractional vaporization of 20% of fractionating volume. The black line corresponds to $F_a = F_o$. This is not the same as the black line in Fig. 8 and does not separate the same populations of planets. The gray lines show $10\times$ uncertainty.

Because Reactions 1 & 2 involve water, they occur more readily where water content is enhanced: e.g. beyond the snowline or in objects that accrete material from beyond the snowline. Consistent with this, rocky objects that formed further out in the solar nebula have more mantle FeO(T) (Fig. 7) (Rubie et al. 2011, 2015). With 18 wt% FeO in silicates, Mars is (just) unstable to stratification under fractional vaporization (although only for relatively cool magma) (Fig. 7). FeO-rich silicate compositions (>25 wt%) are also obtained for the parent body of the CI-class meteorites, the parent body of the CM-class meteorites, and some angrite-class meteorites (Anders & Grevesse 1989; Lewis 2004; Keil 2012). Planets with even more FeO are theoretically reasonable, and Ceres may be a solar system example (Ciesla et al. 2015; Elkins-Tanton & Seager 2008a; McCord & Sotin 2005; Rubie et al. 2015). [FeO] can affect hot-rocky-planet atmospheric thickness and time variability (Figs. 2, 7). Because atmospheric thickness and magma-planet variability are potentially observable, this suggests a route to constrain hot-rocky-planet composition. Such routes are valuable, because mass and radius measurements only weakly constrain the composition of exoplanet silicates (Dorn et al. 2015; Fogtman-Schulz et al. 2014; Gong & Zhou 2012; Rogers & Seager 2010).

Furthermore, because water is less available inside the snowline, [FeO] probes the hot rocky planet’s birth location relative to the snowline (and thus migration distance). Assuming a radial temperature gradient similar to the solar nebula, and further assuming that only a negligible fraction of Fe-silicates from the birth molecular cloud (Jones 1990; Min et al. 2007) survive to be incorporated into hot rocky exoplanets, evidence for mantle [FeO] in hot rocky exoplanets is evidence against in-situ accretion (Chiang & Laughlin 2013). Evidence for mantle [FeO] in hot rocky exoplanets might be used to test inside-out planet formation (Chatterjee & Tan 2014). This is because [FeO] formation in the Solar System occurred on $>km$ -sized objects, but in the Chatterjee & Tan (2014) model, $>km$ -sized objects are assembled close to the star from dehydrated boulders. If hot rocky exoplanets formed through migration of objects of planetesimal size or larger from beyond the snowline (Cossou et al. 2014; Raymond et al. 2014), then we expect high [FeO] on hot rocky exoplanets.

4. DISCUSSION.

4.1. Overview of Approximations & Model Limitations.

Our model omits or simplifies geologic processes that are not well understood even for the rocks of Earth. For example, two-phase (mush) effects, such as magma solitons, filter-pressing, and fingering instabilities (Scott & Stevenson 1984; Katz et al. 2006; Solomatov 2015), are not included in our model. Melt-residue separation at modest temperatures (low melt fractions) will yield Ca-rich, Al-rich melts. Ca/Al-rich melts have low T_{lo} , and tend to favor overturning during fractional vaporization. This overturning-promoting effect is less strong for the high melt fractions (hot rocky exoplanets) that are considered here. However, even at high melt fraction, olivine separation from melt might still be important, and the effect of this process on surface composition could be a target for future work (Asimow et al. 2001; Suckale et al.

2012).

Bulk-rock compositions are assumed to be similar to Solar System silicates, consistent with rocky planet densities, stellar spectra, and white-dwarf data (Dressing et al. 2015; Jura & Young 2014; Lodders et al. 2009; Thiabaud et al. 2015; Adibeykan et al. 2015; Gaidos 2015). Some accretion simulations predict strongly varying Mg/Si (Carter-Bond et al. 2012; Carter et al. 2015). Future work might compute $(\rho_0 - \rho_h)$ for a broad range of silicate composition (Fig. 7).

We assume a well-stirred mantle. Well-stirred mantles are predicted for large, hot planets by simple theories. Simple theories are undermined by ^{142}Nd and ^{182}W anomalies, which show that the Early Earth’s mantle was not well-stirred (Carlson et al. 2014; Debaille et al. 2013; Rizo et al. 2016). This is not understood.

We do not discuss loss of atmophiles (i.e. primary and outgassed atmospheres), oceans and crust (Lupu et al. 2014). These steps should complete in < 1 Ga even if the efficiency of EUV-driven atmospheric escape is low, although CO_2 might resist ablation through $4.3 \mu\text{m}$ -band cooling (Tian et al. 2009; Tian 2015). Fig. 19 shows results of a sensitivity test for crustal evaporation.

We also do not pursue the question of what happens to the magma-pool circulation on planets where the magma-pool circulation is dominated by the mass loading of atmospheric condensates (Tokano & Lorenz 2016). Such mass loading could throw the magma-pool circulation into reverse, but only on strongly atmosphere-dominated planets where the magma-pool circulation is much less efficient at transporting heat than is the atmosphere.

The atmospheric model has several limitations: (1) We assume that the temperature of evaporating gases is equal to the substellar temperature. (2) The model assumes a single atmospheric species. Although a single species typically dominates the silicate atmosphere (Schaefer & Fegley 2009), real atmospheres have multiple species. This is not a big problem in the evaporation zone (where the *total* saturation vapor pressure exceeds the *total* pressure of the overlying atmosphere). However, in the condensation zone, less-refractory atmospheric constituents form a diffusion barrier to condensation, so condensation-zone pressures will be higher in reality than in our model. This could increase P at θ_p . (3) Feedbacks between X_s and $P(\theta)$ during surface compositional evolution are neglected. (4) Magnetic effects (Batygin et al. 2013; Rauscher & Menou 2013; Koskinen et al. 2014) are not included. Thermal ionization reaches $\sim 10^{-3}$ (fractional) at 3100K for Bulk Silicate Earth. (5) We find the initial winds, not the more complex wind pattern that may subsequently develop after compositional variegation develops. (6) Our model lacks shocks (Heng 2012).

Io’s atmosphere is the best solar system analog to magma-planet atmospheres. Over most of Io’s dayside, the approach of Ingersoll (1989) matches Io-atmosphere data (Jessup et al. 2004; Walker et al. 2012). Walker et al. (2010) find (in a sophisticated model that includes both sublimation and volcanic loading) that Io’s atmosphere’s evaporation zone extends 45° - 105° from the substellar point, which is more than predicted by Ingersoll (1989).

Crystallization is inevitable near the edge of a compositionally-evolved pool, because T_{lo} is only just above the $\text{CaO-Al}_2\text{O}_3$ solidus (Berman et al. 1983; Mills et al. 2014). If crystals are small enough to remain entrained in the melt, then evolved fluid near the margin of the pool will increase in density and sink (increased buoyancy forcing in Eqn. 5). If crystallization increases viscosity, then drainage of dense, evolved material into the solid mantle will slow, increasing the likelihood that the surface will have time to evolve into a $\text{CaO-Al}_2\text{O}_3$ -rich composition. Lag formation is hard to avoid if the entire melt pond freezes.

We do not consider light scattering by rock clouds (Juhász et al. 2010). Cloud grain-size depends on P (and thus T_s), so feedbacks involving silicate-dust clouds may modulate magma pool activity (Rappaport et al. 2012).

Thermo-chemical boundary layers can have a complex substructure, which we simplify. Thermal stirring will tend to mix the boundary layer in the small-scale convection zone $\theta > \theta(T_s = \bar{T})$, inhibiting compositional-boundary-layer development. Therefore, development of a buoyant layer segregation is most likely if the compositional boundary layer is developed before $\theta > \theta(T_s = \bar{T})$. This effect reduces the critical τ_X/τ_T by a factor of ~ 2 (within the gray bars in Figs. 8 and 9).

We do not consider how condensed volatiles might return to the pool by gravity-current flow of viscous condensates from the permanent nightside back into the light (Leconte et al. 2013). For example, the Na from Earth corresponds to a hemispheric sheet of thickness 80 km, thick enough to flow back onto the light-side (Leconte et al. 2013). Sublimation of this Na flow might allow an Na-dominated (and thus much thicker) atmosphere to persist even after Na has been removed from the silicate mantle. Analogous flow may occur for S, which is the dominant volatile on Io’s surface and makes up 250 ppm of Earth’s mantle (McDonough & Sun 1995). Escape-to-space is necessary to finally remove these materials from the planet.

For $T_s > 3500\text{K}$, atmospheric heat transport melts the nightside, and the magma pool covers the entire surface – a magma sea. This limit is reached for accreting planets (Lupu et al. 2014; Kuwahara & Sugita 2015; Hamano et al. 2015), planets around post-main-sequence stars, and the hard-to-observe rock surfaces of planets with thick volatile envelopes (e.g. Chen & Rogers 2016; Owen & Morton 2016; Howe & Burrows 2015).

4.2. Albedo Feedbacks.

Only a few relevant albedo measurements exist (Gryvnak & Burch 1965; Adams 1967; Petrov 2009; Nowack 2001), so albedo-composition feedbacks are not considered in detail in this paper. High surface albedo would reduce atmospheric P and mass fluxes, so magma currents are relatively more important on high-albedo worlds. Limited data (Zebger et al. 2005) indicate increasing UV/VIS reflectance with increasing CaO/SiO_2 ratio in the system $\text{CaO-Fe}_2\text{O}_3\text{-SiO}_2$. Taken at face value, these results suggest CaO-rich surfaces could explain data that have been interpreted as indicating high magma-planet albedos (e.g. Rouan et al. 2011; Demory 2014). Per our calculations, CaO-rich surfaces indicate FeO-rich initial

compositions. In turn, this is a strike against in-situ planet formation. This argument is necessarily speculative, because of the paucity of relevant lab data. Motivated by the connection between magma planet albedo and planet formation theory, gathering more laboratory data relevant to magma-planet albedos could make these arguments more rigorous.

4.3. Links to the Solid Mantle: Tectonic Refrigeration.

On Earth, horizontal convection fills the deep sea with cool fluid (Hughes & Griffiths 2008; Lodders & Fogarty 1998). Therefore, Earth’s sea-floor temperature is $\sim 1^\circ\text{C}$, even though Earth’s mean sea-surface temperature is 18°C . Similarly, magma-pool downwellings irrigate the magma-solid interface (“sea-floor”) with cool magma. Cool-magma downwellings set a low and uniform top temperature boundary condition on the dayside mantle circulation. For a dayside-spanning shallow magma pool, the mean temperature at the upper boundary of a convecting-mantle simulation is the mean of the pool-edge temperature T_{lo} and the antistellar-hemisphere surface temperature T_{AS} , i.e., $\sim 850\text{K}$ (Fig. 10). This is because T_{lo} is the characteristic temperature for the magma-solid interface, and magma floods the dayside, while the nightside remains very cold. Because mantle convection (in the absence of tidal heating) will transport much less heat than magma currents, this is a constant- T boundary condition. These low temperatures make 1:1 synchronous rotation more likely, because pseudo-synchronous rotation requires a hot ($> T_{lo}$) interior (Makarov 2015). The “tectonic refrigeration” effect is large (Fig. 10). Convection models (Tackley et al. 2013; Foley et al. 2012; Miyagoshi et al. 2014; O’Rourke & Korenaga 2012; Lenardic & Crowley 2012; van Summeren et al. 2011) could investigate the effects of a hemispherically-uniform upper temperature boundary condition on mantle convection.

4.4. Stratification Should Be Common if Small-Radius Exoplanets Have Outgassed Atmospheres.

Planet density decreases with increasing planet radius in the range $1 < r_{\oplus} < 4$ (Wu & Lithwick 2013; Weiss & Marcy 2014). This density trend can be simply explained by models in which small planets consist of varying proportions of Earth-composition cores and H_2 -rich envelopes (Hadden & Lithwick 2014; Lissauer et al. 2014; Lopez & Fortney 2014; Dressing et al. 2015; Wolfgang et al. 2015). H_2 -rich envelopes might form by nebular accretion (Lee et al. 2014; Bodenheimer & Lissauer 2014; Inamdar & Schlichting 2015; Jin et al. 2014; Ogihara et al. 2015), or by outgassing of H_2 -rich material (Elkins-Tanton & Seager 2008b; Sharp et al. 2013; Sleep et al. 2004). The hottest rocky exoplanets either fail to develop a H_2 -rich envelope, or lose H_2 in < 1 Gyr (Schlichting 2014; Ogihara et al. 2015; Chatterjee & Tan 2014; Lopez & Fortney 2014; Chiang & Laughlin 2013). The upper limit on H_2 outgassing via iron oxidation, corresponding to $[\text{FeO}(\text{T})] = 48.7 \text{ wt}\%$ (Table 2), is $1.7 \text{ wt}\%$ (Rogers et al. 2011). $1.7 \text{ wt}\% \text{H}_2$ is not very much greater than the amount required to explain the radii of low-mass Kepler planets (Lopez & Fortney 2014; Wolfgang & Lopez 2015; Howe & Burrows 2015). Therefore, if outgassing explains the observed radii of Kepler Super-Earths, then

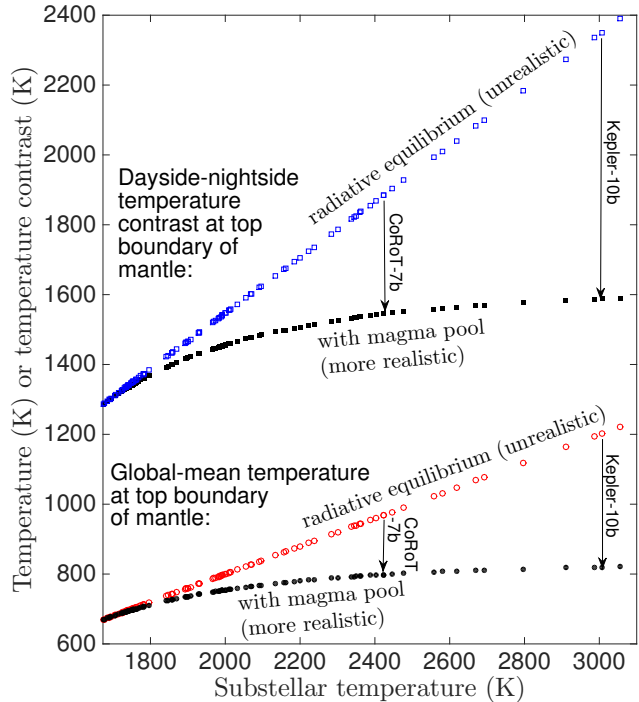


FIG. 10.— Tectonic refrigeration. Upper symbols (squares) show the inter-hemispheric (dayside-nightside) temperature contrast at the top boundary of the solid mantle for hot rocky exoplanets. Black filled squares correspond to a circulating magma pool; blue open squares correspond to the unrealistic case of radiative equilibrium. The lower symbols (circles) show the global mean upper temperature boundary condition for mantle circulation on hot rocky exoplanets. Black filled squares correspond to a circulating magma pool; blue open squares correspond to the unrealistic case of radiative equilibrium. Global mean upper temperature boundary conditions for mantle convection on rocky planets with 1-day periods are not much greater than Venus’ surface temperature (735K).

their rocky cores must contain abundant $\text{FeO}(\text{T})$. Upon H_2 removal via photo-evaporation and impact erosion (Schlichting et al. 2015), the rocky cores of the most-oxidized planets may develop stratified surfaces (Fig. 4), forming a $\text{CaO-Al}_2\text{O}_3$ -rich lag. This is speculative because the percentage of oxidation needed to match Kepler data depends on the molecular weight of the outgassed atmosphere, and this is poorly constrained. The lag might be detectable through its effect on albedo (e.g. Demory 2014) and atmospheric composition.

4.5. Size Dependence & Planet Disintegration.

The molten surfaces of disintegrating rocky planets are the single most likely source for time-variable dust plumes orbiting KIC 12557548, KOI - 2700, K2-22, and WD 1145+017 (Rappaport et al. 2012; Sanchis-Ojeda et al. 2015; Rappaport et al. 2014; Vanderburg et al. 2015). Planet disintegration involves vapor pressures $\gtrsim O(1) \text{ Pa}$ (Perez-Becker & Chiang 2013). Because evolved-surface-composition worlds usually have lower vapor pressures (Fig. 2), they usually resist disintegration. Therefore, observed disintegrating planets require active surface-interior exchange, or entrainment of solids by escaping gas.

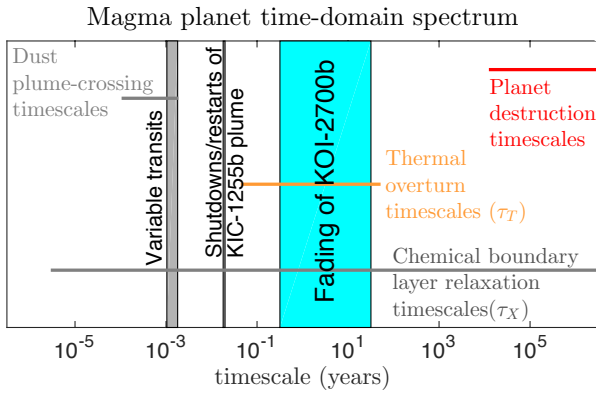


FIG. 11.— Observed magma-planet time variability, compared to possible source mechanisms. Dust plume-crossing timescale from Rappaport et al. (2012). Planet destruction timescale from Perez-Becker & Chiang (2013), assuming 2145 K isothermal Parker wind and vaporization of pure olivine. The left edge of the red bar is for destruction of a 100km-radius planet. Timescales for thermal-overturn (τ_T) and chemical boundary layer relaxation (τ_X) from this paper.

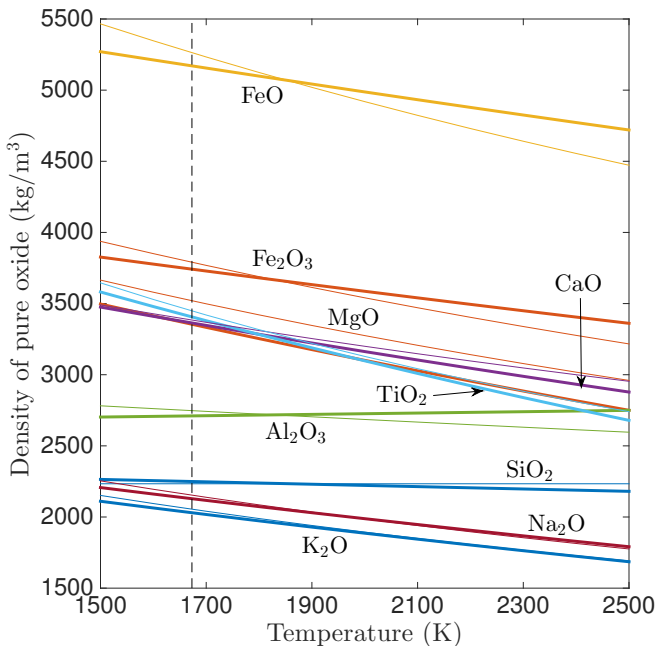


FIG. 12.— Densities of pure oxides according to the fits of Lange & Carmichael (1987) (thin lines) and Ghiorso & Kress (2004) (thick lines). Error bars not shown. Vertical dashed line corresponds to T_{lo} .

Smaller-radius worlds (e.g. KIC 12557548b, KOI-2700b, K2-22b) are more likely (relative to other worlds with the same temperature) to be atmosphere-dominated in our model. This is because the same gradient in atmospheric pressure with angular separation from the substellar point ($\partial P/\partial \theta$) corresponds (for smaller-radius worlds) to a larger mass flux $\frac{\partial M}{\partial x} \propto \nabla(P/rg) \propto r^{-3}$ (Seager et al. 2007). Larger atmospheric mass fluxes favor variegated, time-variable surfaces.

5. IMPLICATIONS FOR OBSERVATIONS.

Current observatories can demonstrably constrain magma-planet time-variability, and place limits on magma-planet albedo (Rouan et al. 2011; Léger et al. 2011; Demory 2014; Dragomir et al. 2014; Sheets & Deming 2014; Rappaport et al. 2012; Sanchis-Ojeda et al. 2015; Rappaport et al. 2014; Vanderburg et al. 2015). VLT/UVES data set upper limits on Ca I, Ca II, and Na in the atmosphere of CoRoT-7b (Guenther et al. 2011). 55 Cnc e, which orbits a $V=6$ star at 12 pc, is the most attractive candidate for magma planet observations currently (Dragomir et al. 2014; Demory et al. 2016a). TESS should increase the number of known nearby magma planets (Sullivan et al. 2015), given a Kepler-based estimate of 6×10^{-4} for magma planet frequency (Ito et al. 2015). Here we outline the implications of magma pool composition for (in turn) observations of the exosphere + upper atmosphere, lower atmosphere/clouds, surface, and time domain. Our discussion draws on the work of Samuel et al. (2014) and Ito et al. (2015).

Magma planet exospheres, upper atmospheres, and dust tails are mainly seen in transit. For the Na resonance doublet, assuming HST/STIS resolution, one can expect to see variations of ~ 5 scale heights in a cloud-free atmosphere (giving 10-15 ppm signal for 55 Cnc e). With HST/STIS, detection of this signal would require ~ 100 transits (scaling from Charbonneau et al. 2002). But the signal is easily detectable in a single transit with HST/STIS (3000 ppm) if the Na (or K) absorption extends to fill the $\sim 3 R_p$ Hill sphere of 55 Cnc e. JWST/NIRSPEC should improve over HST/STIS for magma planet observations. (This improvement is hard to quantify because JWST/NIRSPEC error for bright stars may be dominated by systematics.) Na detection would indicate that the planet's surface is little-fractionated. [FeO] might be constrained by dust-tail spectroscopy (Croll et al. 2014, 2015; Bochinski et al. 2015).

Magma planet clouds and lower-atmospheres can be observed using secondary-eclipse spectroscopy. Ito et al. (2015) find that a photon-limited JWST-class telescope can detect SiO, Na and K in the atmosphere of 55 Cnc e with 10 hours of observations. Albedo measurements are possible at lower S/N; they may correspond to the albedo of clouds, or the albedo of the surface (Rouan et al. 2011; Dragomir et al. 2014; Demory 2014).

Illustrating the imminent detectability of magma-surface properties, a phase curve for 55 Cnc e was reported while this paper was in review (Demory et al. 2016a). The phase curve shows a $\sim 40^\circ$ eastward hotspot offset and an antistellar-hemisphere temperature of ~ 1400 K. This high antistellar-hemisphere temperature requires heat transport (§2). Transport by magma currents is insufficient to explain the antistellar-hemisphere temperature (Fig. 9), so an atmosphere is indicated. 55 Cnc e's density is consistent with an Earth-like composition (Demory et al. 2016a), but the planet may nevertheless have retained an envelope of non-silicate volatiles. Near-future instruments (e.g. NIRSPEC on JSWT) can measure CoRoT-7b's Bond albedo to ± 0.03 , test the synchronous-rotation assumption, and set limits on atmospheric density (Samuel et al. 2014). This will help to distinguish the compositionally-evolved from the compositionally-primitive endmembers discussed in

this paper (Fig. 2).

Disintegrating magma planets have dust plumes that are time-variable (Fig. 11). Short-timescale variations are plausibly linked to limit cycles involving the dust-plume optical depth and the surface magma temperature (Perez-Becker & Chiang 2013). However, longer-timescale variations (e.g. quiescent periods, Rappaport et al. 2012; van Werkhoven et al. 2014) must be rooted in a reservoir with a correspondingly longer relaxation time, such as the magma pool. For example, KOI-2700b’s dust cloud faded from 2009-2013 (Rappaport et al. 2013). This may be connected to the magma-pool thermal-overturn timescale τ_T , which is usually a few years (Figs. 8, 11). On this timescale, a patch of pool surface that is anomalously-dark (thus hot, with increased gas output) will drift to the pool edge and subside. High-[FeO] worlds have stable surfaces (Fig. 7), so any light-side transient implies low [FeO]. From Fig. 8, period $p > 1.5$ day magma planets ($p > 1$ day for albedo 0.5) should lack surface-driven variability on timescales $< 10^6$ s.

We conclude our discussion of observability with observational possibilities that are intriguing, but less likely. The induced power from a ring of metal (e.g. Na, Fe ...) condensed just beyond the terminator might affect magnetism. J_2 constraints (Batygin et al. 2009) are unlikely to break degeneracies because of the trade-off between unknown mantle FeO and unknown planet Fe/Si (Taylor & McLennan 2009). Ito et al. (2015) state that planetary radial velocities (i.e. wind speeds) are marginally detectable for Na and K for a telescope of the class of Giant Magellan Telescope. Direct proof of fractional vaporization might involve measurement of isotopomers of SiO (Campbell et al. 1995).

6. CONCLUSIONS.

Magma-pool overturning circulation and differentiation represents a new tectonic mode for rocky planets at temperatures too high for plate tectonics, stagnant-lid convection, or heat-pipes (Korenaga 2013; Stamenković & Breuer 2014; Sleep 2000; Moore & Webb 2013).

Surface-interior exchange on hot rocky exoplanets is driven by near-surface contrasts in melt density (and can shut down if the surface layer becomes stably buoyant). In turn, these density effects are regulated by two factors (Fig. 7).

1. *Relative vigor of evaporation and circulation.* For “magam-pool-dominated” worlds (substellar temperature $\lesssim 2400\text{K}$), magma-pool overturning circulation outruns net evaporation. Pool surface composition tracks bulk-pool composition. For “atmosphere-dominated” worlds (substellar temperature $\gtrsim 2400\text{K}$), pool overturning circulation is slow compared to atmospheric transport. Fractional evaporation drives pool-surface composition away from the composition of the bulk of the pool.
2. *Exposure of the planet’s building-blocks to oxidants such as H_2O .* If the planetesimals that formed the planet grew $\gtrsim 1$ AU from the star, water-rock reactions will lead to high Fe-oxide concentrations in the planet’s silicate mantle. Close to the star, preferential evaporation of volatile and dense Fe

favors stable stratification of the residual magma. This may allow a buoyant, stable lag to form – a compositionally-evolved surface. However, if the planetesimals that formed the planet are more reduced, fractionally-evaporated residual melt will sink. The concomitant resurfacing will repeatedly reset the surface composition to the planet-averaged silicate composition.

We thank Bruce Buffett, Michael Manga, Ruth Murray-Clay, Paul Asimow, Larry Grossman, Diana Dragomir, Valeri Makarov, Dorian Abbot, Michael Efroimsky, Ray Pierrehumbert, Eric Ford, Bethany Ehlmann, Brice-Olivier Demory, and especially Jacob Bean and Malte Jansen for discussions. We thank the anonymous reviewer and the editor, Steinn Sigurdsson. B.F. was supported by NSF grant AST-1412175. E.S.K. thanks the Astrophysics and Geosciences Departments at Princeton University for providing financial support and a convivial home while the ideas in this paper were marinating.

APPENDIX

A. MATERIAL PROPERTIES.

Density. We obtain molar volumes for melts in the early stages of fractionation from the silicate-melt equation of state of Ghiorso & Kress (2004) (Fig. 12). This EoS is calibrated against a wider range of experiments, and so is preferred to, the EoS of Lange & Carmichael (1987). Mixture densities assume ideal mixing (Bottinga & Weill 1970); nonideal-mixing density errors are small for early-stage fractionation. Ghiorso & Kress (2004) include a fictitious “book-keeping” oxide, $\text{FeO}_{1.3}$, which we ignore; the inclusion of this fictitious oxide would make FeO-rich silicates even denser and therefore would not alter our conclusions. Both equations of state assume constant $\partial V/\partial T$, consistent with simulations (Guillot & Sator 2007).

Late stages of fractionation produce CaO - MgO - Al_2O_3 - SiO_2 (CMAS) melts. The Ghiorso & Kress (2004) and Lange & Carmichael (1987) models are not calibrated for these melts (Fig. 13). Instead, we use the CMAS equation-of-state of Courtial & Dingwell (1999), including their SiO_2 -CaO nonideal-mixing term. To check, we compare to the data of Courtial & Dingwell (1995), Courtial & Dingwell (1999) (both using the double-bob Archimedean method), and Aksay et al. (1979). Errors are small, as expected, except for densities measured with the X-ray radiography method (Aksay et al. 1979). A switch from four-oxygen to six-oxygen coordination of Al at high Al contents increases the density of Al-rich melts (Jakse et al. 2012).

Molecular diffusivity. Diffusivity in the melt, κ_X is set to $2.8 \times 10^{-7} \exp(-7.9 \times 10^{-4} \mu_l^{-1} / (8.314 \mu_l^{-1} \bar{T}))$. $\mu_l = 100$ g is the assumed molar mass in the liquid. This follows simulations of Mg self-diffusion in hydrous melts by Karki et al. (2010), but reduced by a factor of 2 to take account of anhydrous effects, per de Koker & Stixrude (2011). There is only a small dependence on component mass (Tsuchiyama et al. 1994). Using self-diffusivities is an approximation to the real, multicomponent diffusion. Self-diffusivities at 3000K are slightly lower for O than for Mg, and ~ 3 times lower for Si than for Mg.

TABLE 3
PREDICTIONS OF ATMOSPHERIC PRESSURE AND SURFACE COMPOSITION FOR SELECTED MAGMA PLANETS.

Planet	p (d)	T_{ss} (K)	Melt pool radius ($^\circ$)	Mean pool temperature \bar{T} (K)	Pool depth ($\delta_p \times 10$) (m)	$(\theta_p > \theta_0)$?	Pool-overturn timescale (s)	Atmosphere timescale (s)	P_{ss} at 95 wt% fractionation (Pa)	P_{ss} at 20 wt% fractionation (Pa)
<i>Not known to be disintegrating:</i>										
CoRoT-7b	0.85	2425	77 $^\circ$	2146	100	Y	10 ⁸	<u>10⁷</u>	10 ⁰	10 ²
55 Cnc e	0.74	2671	88 $^\circ$	2263	200	Y	10 ⁹	<u>10⁶</u>	10 ¹	10 ³
Kepler-36b	13.8	1476	0 $^\circ$	n.a.	n.a.	n.a.	n.a.	n.a.	<10 ⁻⁸	10 ⁻⁵
Kepler-93b	4.73	1569	0 $^\circ$	n.a.	n.a.	n.a.	n.a.	n.a.	<10 ⁻⁷	10 ⁻⁴
Kepler-78b ^a	0.36	3056	102 $^\circ$	2423	200	Y	10 ⁹	<u>10²</u>	10 ²	10 ⁴
Kepler-10b	0.84	3007	96 $^\circ$	2464	200	Y	10 ⁹	<u>10³</u>	10 ²	10 ⁴
<i>Disintegrating:</i>										
KIC 12557548b	0.65	2096	66 $^\circ$	1919	100	Y	10 ⁸	<u>10⁷</u>	10 ⁻²	10 ⁰
K2-22b	0.62	2135	68 $^\circ$	1945	100	Y	10 ⁹	<u>10⁶</u>	10 ⁻²	10 ⁰
KOI-2700b	0.91	1780	39 $^\circ$	1730	60	Y	<u>10⁸</u>	10 ¹¹	10 ⁻⁵	10 ⁻²

NOTE. — Dominant timescales are underlined. Timescales calculated for 20 wt % fractionation. An initial composition corresponding to that of Bulk Silicate Earth is assumed. Pressures $< O(1)$ Pa are too low for disintegration (Perez-Becker & Chiang 2013).

^a The assumptions made in obtaining the atmosphere and ocean timescales are only marginally satisfactory for planets as hot as Kepler-78; see §3.3.

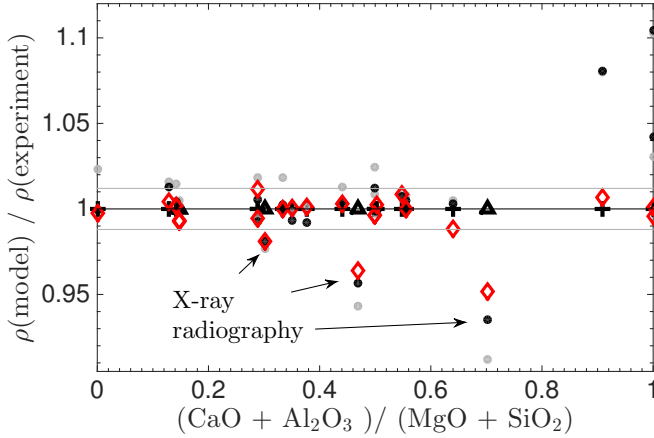


FIG. 13.— Comparison of models to data for the CaO-MgO-Al₂O₃-SiO₂ system (appropriate for high degrees of fractional vaporization of silicate magmas). Crosses correspond to experiments using the double-bob Archimedean method. Triangles correspond to X-ray radiography experiments. Dots and diamonds correspond to modelled densities: gray dots for the model of Lange & Carmichael (1987); black dots for the model of Ghiorso & Kress (2004); and red diamonds for the model of Courtial & Dingwell (1999). Error bars on the experiments (not shown) are small compared to the mean data-model discrepancy.

Diffusivity in the solid (κ_S) is $\lesssim 10^{-14} \text{ m}^2 \text{ s}^{-1}$ for olivine at $\sim 1700\text{K}$ (Brady & Cherniak 2010). For example, Chakraborty (2010) reports $\kappa_S \sim O(10^{-14}) \text{ m}^2 \text{ s}^{-1}$ at $\sim 1770 \text{ K}$ for Mg diffusion in olivine (and $\kappa_S < 10^{-17} \text{ m}^2 \text{ s}^{-1}$ for Si and O). Similarly low values are reported for Mg diffusion in periclase (Van Orman & Crispin 2010), so the true Lewis number may be even lower than used here.

Liquidus temperature and lock-up temperature. The Katz et al. (2003) crystallization-temperature parameterization interpolates between “0 GPa” experiments carried out on a rock that is representative of Earth’s mantle: KLB-1 peridotite (Takahashi 1986). Katz et al. (2003) recommends a parameterization that yields 1673

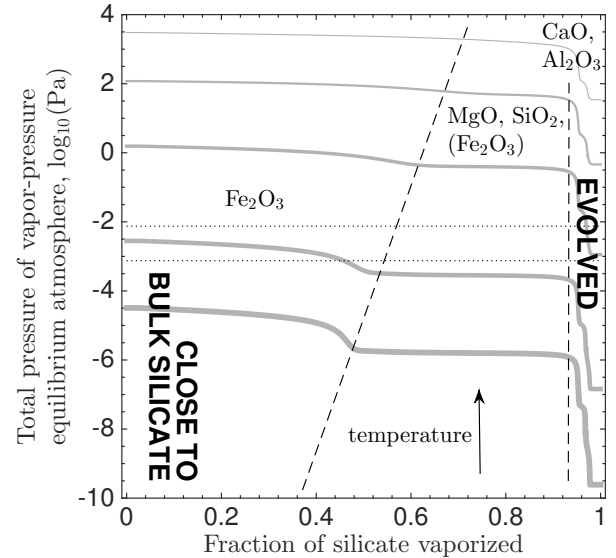


FIG. 14.— Fractional vaporization of a “coreless” exoplanet (Elkins-Tanton & Seager 2008a). The gray lines correspond to atmospheric pressure at temperatures of 1400K, 1600K, 2000K, 2400K, and 2800K (in order of decreasing line thickness). The vertical dashed lines separate regions where different oxides (text) control the density-evolution of the residual fluid. The horizontal dotted lines show the pressure below which UV-driven escape is less efficient (optical depth = 1 for surface gravities of 1.5 m s^{-2} (lower dotted line) and 15 m s^{-2} (upper dotted line), assuming molar mass 30 Da and photoabsorption cross-section of $10^{-22} \text{ m}^2 \text{ molecule}^{-1}$; Reilman & Manson (1979)).

K for T_{lo} .

B. DEPTH OF THE MELT POOL IN THE ABSENCE OF AN OVERTURNING CIRCULATION.

Combining the effects of pressure-induced crystallization and the cooling of near-surface material by underlying cooler solid mantle, the bottom boundary of the melt pool is the depth where $T(z) = T_{lo}(z)$. This depth is

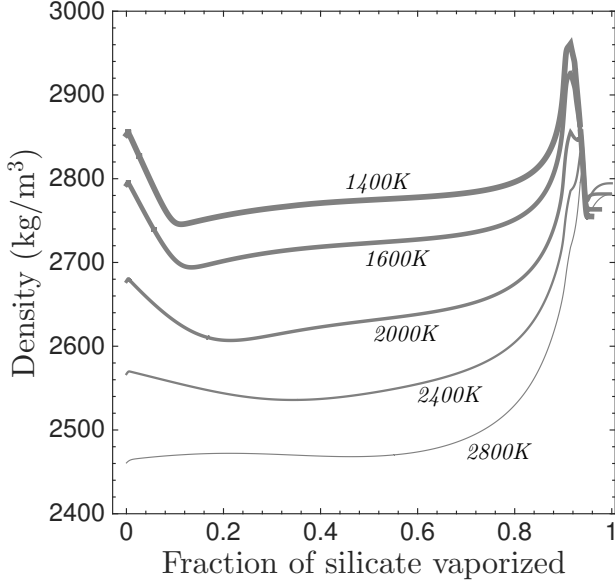


FIG. 15.— Residual-magma density evolution for fractional vaporization of an initial composition corresponding to Bulk Silicate Earth.

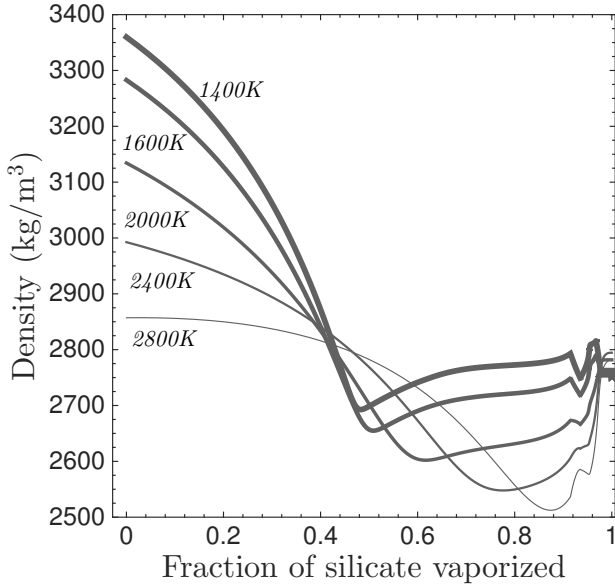


FIG. 16.— Residual-magma density evolution for fractional vaporization of an initial composition corresponding to a “coreless” exoplanet (Elkins-Tanton & Seager 2008a). The wiggles around 93 wt% fractionation are artifacts caused by the transition in our model from the Ghiorso & Kress (2004) equation-of-state to the Courtial & Dingwell (1999) equation-of-state.

given by

$$d_p \approx d_{bl} \frac{\bar{T} - T_{lo}(z)}{d_{bl} (\partial T_{lo} / \partial z) + (\bar{T} - T_{mantle})} \quad (\text{B1})$$

where \bar{T} is the surface temperature of a well-stirred pond, $\bar{T} = (T_{ss} \pi \sin^2 \theta_p) / 2\pi (1 - \cos \theta_p)^{1/4}$, and d_{bl} is the thickness of the mantle boundary layer. Because pressure favors crystallization, $T_{lo}(z)$ increases with depth:

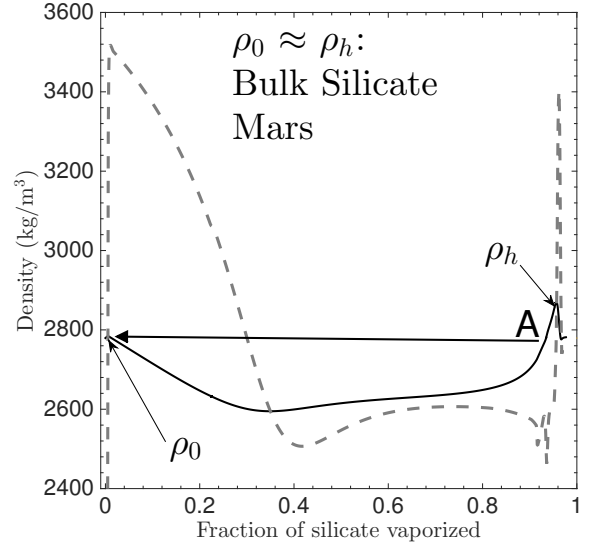
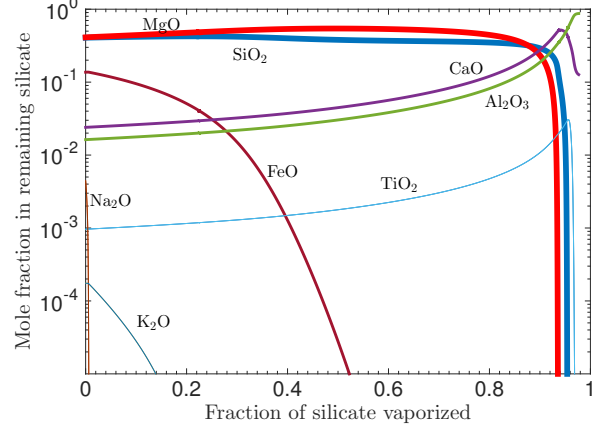


FIG. 17.— Fractional vaporization (at 2000K) of an initial composition corresponding to Bulk Silicate Mars. *Upper panel*: Residual-magma compositional evolution. *Lower panel*: Density evolution. Thin black solid curve corresponds to the density of residual magma, and thick gray dashed curve corresponds to the density-upon-condensation of the gas. ρ_0 corresponds to unfractionated magma density. ρ_h corresponds to the maximum density at >70 wt% fractional vaporization. At point A, the surface boundary layer is unstable to sinking. For Bulk Silicate Mars initial composition, the density-upon-condensation curve is truncated at 0.97, due to numerical artifacts beyond 0.97.

$(\partial T_{lo} / \partial z) = 2 \times 10^{-3} \text{ K m}^{-1}$ for $g = g_{\oplus}$ (Solomatov 2015; Sleep 2007). $(\partial T_{lo} / \partial z)$ is proportional to gravity because the adiabatic temperature gradient and the slope of the curve of constant melt fraction are both proportional to pressure (Kite et al. 2009). For $\bar{T} = 2400 \text{ K}$, $T_{mantle} = 1500 \text{ K}$, $d_{bl} = 70 \text{ km}$, Eqn. (B1) gives $d_p \sim 50 \text{ km}$. In reality, lateral flow in the pool further suppresses d_p . Setting $d_{bl} = 70 \text{ km}$ implies mantle circulation speeds of the same order of magnitude as those calculated for Earth (Watters et al. 2009; van Summeren et al. 2011; Gelman et al. 2011).

C. STIRRING THE MELT POOL.

The melt pool overturns more quickly if the effective (molecular or eddy) diffusivity is high. Wind-driven waves can stir the pool, especially if they break. Fol-

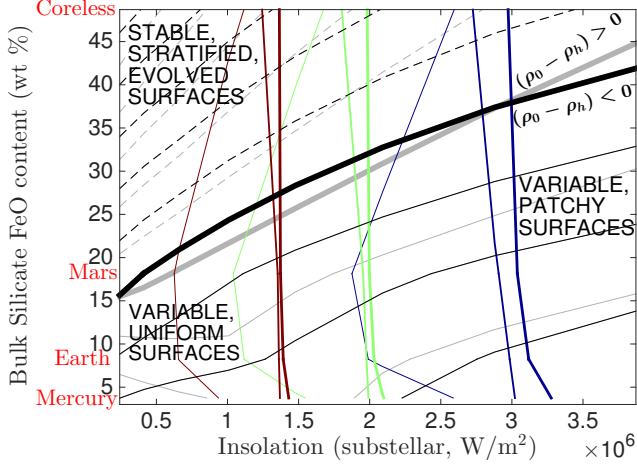


FIG. 18.— Detailed magma planet phase diagram (a simplified version of this figure is shown in Fig. 7). Black and grey lines correspond to stratification index $(\rho_0 - \rho_h)$ contoured at 100 kg m^{-3} intervals. Negative values solid, positive values dashed. The zero line is highlighted by thick black and grey lines. Black contours correspond to the Ghiorso & Kress (2004) equation-of-state, and gray contours correspond to the Lange & Carmichael (1987) equation-of-state (Appendix A). Colored lines correspond to (red lines, left) $\tau_X/\tau_T = 10$, (green lines, middle) $\tau_X/\tau_T = 1$, and (blue lines, right) $\tau_X/\tau_T = 0.1$. Among the colored lines, the thin lines correspond to <1 wt% vaporization, the medium-thickness lines correspond to 50 wt% vaporization, and the thick lines correspond to 80 wt% vaporization. A choice of one colored \sim vertical line and one black-or-gray diagonal line divides the plot into quadrants. Then, the lower-left quadrant corresponds to ocean-dominated planets with uniform, but time-variable surfaces, driven by thermal overturn. The lower-right quadrant correspond to atmosphere-dominated planets with variable, variegated surfaces driven by evaporative overturn. The upper two quadrants correspond to planets with stable, stratified, $\text{CaO-Al}_2\text{O}_3$ -dominated surfaces (compositionally evolved). Calculations assume orbital period $p = 0.84$ days, planet radius $1.47 R_\oplus$, gravity $1.9 g_\oplus$, appropriate for Kepler-10b.

lowing Lorenz & Hayes (2012), transfer of energy J from the atmosphere to the wave-field scales as

$$\frac{\partial J}{\partial x} \sim \frac{1}{2} C_d \rho_a \xi v^2 \quad (\text{C1})$$

where $C_d \approx 2 \times 10^{-3}$ is a surface exchange coefficient (Emanuel 1994), and $\xi \sim 0.01$ is a correction factor for near-surface wind speed. Since $\rho_a \approx P/(gH) \approx 10^{-6} \text{ kg m}^{-3}$, $\partial J/\partial x \sim 10^{-7} \text{ J m}^{-2} \text{ m}^{-1}$, so $E = 1 \text{ J m}^{-2}$ for an $L = 10^7 \text{ m}$ magma pool and a 1 Pa atmosphere. Lorenz & Hayes (2012) give $J = 0.125 \rho_l g h_w^2$, and (ignoring dissipation) this gives a maximum wave height $h_w = 0.015 \sqrt{P}$ m. Therefore waves are unlikely to be big enough to mix the boundary layer, even if they break. An analogy is diapycnal viscosity at Earth’s thermocline ($10^{-5} \text{ m}^2 \text{ s}^{-1}$; Munk & Wunsch (1998)). Stirring will increase if insolation penetrates below the thermocline. We assume insolation is absorbed near the surface, above the thermocline. Increasing stirring has only modest effect on τ_T (100-fold increase in κ_T only increases ocean circulation speeds 4-fold). Faster stirring delays the development of a compositional boundary layer, which would allow thicker atmospheres to persist (Fig. 2). However, because increasing ρ_a also increases E , this is unlikely to shift the boundary between ocean-dominated pools and atmosphere-dominated pools that is shown in Fig. 8.

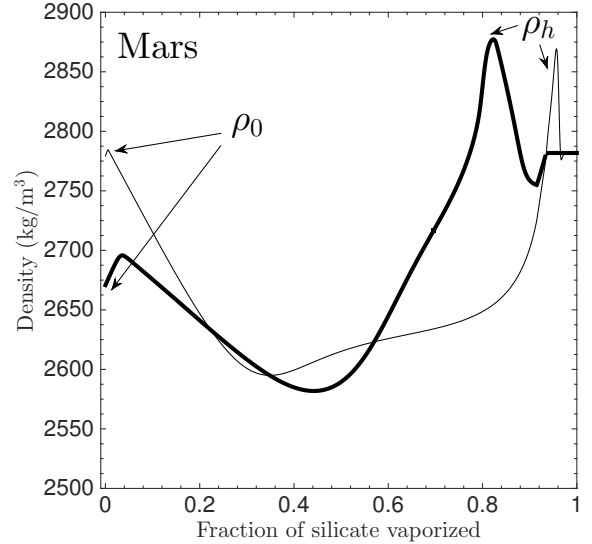
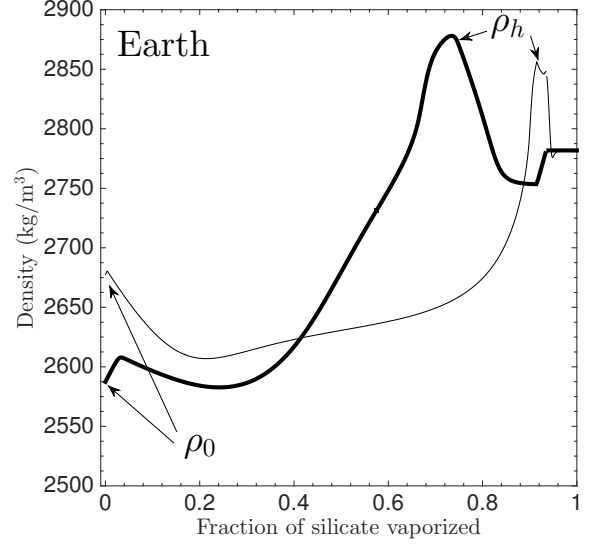


FIG. 19.— Crust-vaporization sensitivity test. Residual-magma density evolution during fractional evaporation of the crust versus mantle, for Earth (*top panel*) and Mars (*lower panel*). Thick lines correspond to fractional evaporation of crust (early stages in planet destruction) and thin lines correspond to fractional evaporation of mantle (later stages in planet destruction). The Earth oceanic crust composition is from Klein (2005) and the Mars crust composition is from Taylor & McLennan (2009); mantle compositions are shown in Table 2. Peak density during fractionation (ρ_h) moves to the left for fractional-evaporation of crust due to the partitioning of Ca and Al into the melt during crust formation; initial densities (ρ_0) are also lower.

Tides can speed up ocean circulation (Munk & Wunsch 1998; Běhouňková et al. 2010, 2011; Jackson et al. 2008; Makarov & Efroimsky 2014; Henning & Hurford 2014). Tidal heating in the solid mantle might allow night-side volcanism (Moore et al. 2007; Tyler et al. 2015). The WASP-47 system may be an example.

D. ATMOSPHERE MODEL: FROM \bar{T} TO τ_X .

Volatile transport by the vapor-equilibrium atmosphere depends on pressure gradients. Equilibrium pressure depends on $\bar{T}_s(\theta)$ and depends on surface composition.

$T_s(\theta)$ is given by:

$$T_s = T_{AS} + \Delta T \cos(\min(\theta, \pi/2))^{1/4}, \quad (\text{D1})$$

where $T_{AS} = 50\text{K}$ is the antistellar temperature corresponding to a geothermal heat flux of 0.35 W m^{-2} , and $\Delta T = T_{ss} - T_{AS}$. In the twilight zone we replace Eqn. D1 with the temperature corresponding to a linear interpolation of the stellar flux (footnote 2). The resulting $T_s(\theta)$ is similar to that in Léger et al. (2011).

Using a uniform-surface-composition assumption to get $P_{eq}(\theta)$ (via Eqn. 12), we next find the wind driven by $\partial P/\partial\theta$, assuming $P \approx P_{eq}$. The wind is assumed to be everywhere directed away from the substellar point. Eqns. (D2 - D5) follow the approach of Ingersoll (1989) (similar to Castan & Menou (2011)). This approach has several limitations, which are discussed in §4.1. Neglecting friction, and assuming injected gas has a constant temperature T_0 , energy conservation yields wind speed v

$$v = \sqrt{2 \left(\frac{c_p T_0}{\mu} - \frac{c_p T(\theta)}{\mu} \right)}; \quad (\text{D2})$$

Temperature is set using

$$\frac{1}{r \sin \theta} \frac{\partial}{\partial \theta} (2c_p(T_0 - T)P \sin \theta) + \frac{1}{r} \frac{\partial}{\partial \theta} (\beta c_p T P) = 0. \quad (\text{D3})$$

Mass conservation constrains sublimation, E (kg m^{-2}

s^{-1}):

$$E = \frac{1}{g r \sin \theta} \frac{\partial}{\partial \theta} (v P \sin \theta); \quad (\text{D4})$$

E is proportional to pressure and to (temperature) $^{1/2}$. We integrate (D2)-(D5) by shooting from $\theta = 0$, with initial conditions $P = P(T_s(\theta = 0))$, $v = 0$, $T = T_0$. Example output is shown in Fig. 6.

The switch from evaporation to surface condensation occurs at $\theta_0 = (35 \pm 5)^\circ$. θ_0 is insensitive to T_s , $P(\theta = 0)$, or X_s . Therefore, chemical fractionation (lower P) does not change the basic evaporation-condensation structure shown in Fig. 6.

Maintaining a sublimation flux E requires a fractional deviation from the equilibrium pressure of

$$\frac{\Delta P}{P} \approx \frac{-E \sqrt{2\pi R T / \mu}}{\gamma P(T_s(0))} \quad (\text{D5})$$

(the Hertz-Knudsen equation), assuming a single-component system, with the evaporation coefficient $\gamma \sim 0.03\text{-}0.3$ near the liquidus, and rising with temperature (Tsuchiyama et al. 1999; Grossman et al. 2000; Alexander 2001; Richter et al. 2002; Lauretta et al. 2006; Fedkin et al. 2006; Richter et al. 2007, 2011); we set $\gamma = 0.2$. We find $\Delta P/P \lesssim 10\%$ ($0.1/\gamma$), validating the approximation $P \approx P_s(T_s(\theta))$. As a second self-consistency check, we feed the latent-heat flux back into the T_s equation (Eqn. D1). Changes in T_s are minor ($<3\%$), except for the hottest planet Kepler-78b.

REFERENCES

- Adams, J. 1967, *J. Quant. Spec. Radiat. Transf.*, 7, 273
 Adibekyan, V., et al., arXiv:1508.04970
 Aksay, I. A., Pask, J. A., & Davis, R. A., *J. of the American Ceramic Society*, 62, 332
 Alexander, C. M. O. 2001, *M&PS*, 36, 255
 Anders, E., & Grevesse, N. 1989, *Geochim. Cosmochim. Acta*, 53, 197
 Asimow, P.D., Hirschmann, M.M., Stolper, E.M., 2001, *J. Petrology*, 42, 963
 Ballard, S., Chaplin, W. J., Charbonneau, D., et al. 2014, *ApJ*, 790, 12
 Batalha, N. M., Borucki, W. J., Bryson, S. T., et al. 2011, *ApJ*, 729, 27
 Batygin, K., Bodenheimer, P., & Laughlin, G. 2009, *ApJ*, 704, L49
 Batygin, K., Stanley, S., & Stevenson, D. J. 2013, *ApJ*, 776, 53
 Běhouňková, M., Tobie, G., Choblet, G., & Čadež, O. 2010, *JGR-Planets*, 115, E09011
 Běhouňková, M., Tobie, G., Choblet, G., & Čadež, O. 2011, *ApJ*, 728, 89
 Berman, R. G., PhD thesis, U. British Columbia, 1983.
 Bochinski, J. J., Haswell, C. A., Marsh, T. R., Dhillon, V. S., & Littlefair, S. P. 2015, *ApJ*, 800, L21
 Bodenheimer, P., & Lissauer, J. J. 2014, *ApJ*, 791, 103
 Bottinga, Y., Weill, D.F. 1970, *Am. J. of Sci.*, 269, 169
 Brady, J.B., & D.J. Cherniak, *Rev. Mineral. Geochem.*, 72, 899-920, 2010.
 Budaj, J., Kocifaj, M., Salmeron, R., & Hubeny, I. 2015, *MNRAS*, 454, 2
 Callegari, N., & Rodríguez, Á. 2013, *Celestial Mechanics and Dynamical Astronomy*, 116, 389
 Campbell, J. M., Klapstein, D., Dulick, M., Bernath, P. F., & Wallace, L. 1995, *ApJS*, 101, 237
 Carlson, R. W., Garnero, E., Harrison, T. M., et al. 2014, *Annual Review of Earth and Planetary Sciences*, 42, 151
 Carter, J. A., Agol, E., Chaplin, W. J., et al. 2012, *Science*, 337, 556
 Carter, P. J., Leinhardt, Z. M., Elliott, T., Walter, M. J., & Stewart, S. T. 2015, *ApJ*, 813, 72
 Carter-Bond, J. C., O'Brien, D. P., & Raymond, S. N. 2012, *ApJ*, 760, 44
 Castan, T., & Menou, K. 2011, *ApJ*, 743, L36
 Chakraborty, S., *Rev. Mineral. Geochem.*, 72, 603-639, 2010.
 Charbonneau, D., Brown, T. M., Noyes, R. W., & Gilliland, R. L. 2002, *ApJ*, 568, 377
 Charpinet, S., Fontaine, G., Brassard, P., et al. 2011, *Nature*, 480, 496
 Chatterjee, S., & Tan, J. C. 2014, *ApJ*, 780, 53
 Chen, H., & Rogers, L. A. 2016, arXiv:1603.06596
 Chiang, E., & Laughlin, G. 2013, *MNRAS*, 431, 3444
 Ciesla, F. J., Mulders, G. D., Pascucci, I., & Apai, D. 2015, *ApJ*, 804, 9
 Cossou, C., Raymond, S. N., Hersant, F., & Pierens, A. 2014, *A&A*, 569, A56
 Correia, A. C. M., Boué, G., Laskar, J., & Rodríguez, A. 2014, *A&A*, 571, A50
 Courtial, P., & Dingwell, D. B. 1995, *Geochim. Cosmochim. Acta*, 59, 3685
 Courtial, P., & Dingwell, D. B. 1999, *American Mineralogist*, 84, 465
 Croll, B., Rappaport, S., DeVore, J., et al. 2014, *ApJ*, 786, 100
 Croll, B., Dalba, P. A., Vanderburg, A., et al. 2015, arXiv:1510.06434
 Dai, F., Winn, J. N., Arriagada, P., et al. 2015, *ApJ*, 813, L9
 Debaille, V., O'Neill, C., Brandon, A. D., et al. 2013, *E&PSL*, 373, 83
 de Koker, N. and L. Stixrude, *Rev. Mineral. Geochem.*, 72, 971-996, 2011.
 Demory, B.-O., de Wit, J., Lewis, N., et al. 2013, *ApJ*, 776, L25
 Demory, B.-O. 2014, *ApJ*, 789, L20
 Demory, B.-O., Gillon, M., de Wit, J., et al. 2016, *Nature*, 532, 207
 Demory, B.-O., Gillon, M., Madhusudhan, N., & Queloz, D. 2016, *MNRAS*, 455, 2018

- Dingwell, D. B., Courtial, P., Giordano, D., & Nichols, A. R. L. 2004, *E&PSL*, 226, 127
- Dorn, C., Khan, A., Heng, K., et al. 2015, *A&A*, 577, A83
- Dragomir, D., Matthews, J. M., Winn, J. N., & Rowe, J. F. 2014, *Formation, Detection, and Characterization of Extrasolar Habitable Planets*, 293, 52
- Dreibus, G., & Wanke, H. 1985, *Meteoritics*, 20, 367.
- Dreibus, G., & Wanke, H. 1987, *Icarus*, 71, 225
- Dressing, C. D., Charbonneau, D., Dumusque, X., et al. 2015, *ApJ*, 800, 135
- Dumusque, X., Bonomo, A. S., Haywood, R. D., et al. 2014, *ApJ*, 789, 154
- Ehrenreich, D., & Désert, J.-M. 2011, *A&A*, 529, A136
- Ehrenreich, D., Bourrier, V., Wheatley, P. J., et al. 2015, *Nature*, 522, 459
- Elkins-Tanton, L. T., & Seager, S. 2008a, *ApJ*, 688, 628
- Elkins-Tanton, L. T., & Seager, S. 2008b, *ApJ*, 685, 1237
- Emanuel, K. A. 1994, *Atmospheric Convection*, Oxford Univ. Press, Oxford, U. K
- Esteves, L. J., De Mooij, E. J. W., & Jayawardhana, R. 2015, *ApJ*, 804, 150
- Fedkin, A. V., Grossman, L., & Ghiorso, M. S. 2006, *Geochim. Cosmochim. Acta*, 70, 206
- Fedkin, A. V., & Grossman, L. 2016, *Meteoritics and Planetary Science*, 51, 843
- Fegley, B., & Cameron, A. G. W. 1987, *E&PSL*, 82, 207
- Fogtman-Schulz, A., Hinrup, B., Van Eylen, V., et al. 2014, *ApJ*, 781, 67
- Foley, B. J., Bercovici, D., & Landuyt, W. 2012, *E&PSL*, 331, 281
- Ford, E. B. 2014, *PNAS*, 111, 12616
- Forget, F., & Leconte, J. 2014, *Philosophical Transactions of the Royal Society of London Series A*, 372, 30084
- Frost, D. J., Mann, U., Asahara, Y., & Rubie, D. C. 2008, *Philosophical Transactions of the Royal Society of London Series A*, 366, 4315
- Früh-Green, G. L., Connolly, J. A. D., Plas, A., Kelley, D. S., & Grobóty, B. 2004, *AGU Geophys. Monograph* 144, 119
- Gaidos, E. 2015, *ApJ*, 804, 40
- Gelman, S. E., Elkins-Tanton, L. T., & Seager, S. 2011, *ApJ*, 735, 72
- Ghiorso, M. S., Kress, V. C., 2004, *Am. J. of Sci.*, 304, 679
- Giordano, D., Russell, J. K., & Dingwell, D. B. 2008, *E&PSL*, 271, 123
- Gong, Y.-X., & Zhou, J.-L. 2012, *Research in Astronomy and Astrophysics*, 12, 678
- Grossman, L., & Larimer, J. W. 1974, *Rev. Geophys. Space Phys.*, 12, 71
- Grossman, L., Ebel, D. S., Simon, S. B., et al. 2000, *Geochim. Cosmochim. Acta*, 64, 2879
- Gryvnak, D.A., & Burch, D.E 1965, *J. of the Optical Society of America*, 55, 625
- Guenther, E. W., Cabrera, J., Erikson, A., et al. 2011, *A&A*, 525, A24
- Guillot, B., & Sator, N. 2007, *Geochim. Cosmochim. Acta*, 71, 1249
- Hadden, S., & Lithwick, Y. 2014, *ApJ*, 787, 80
- Hamano, K., Kawahara, H., Abe, Y., Onishi, M., & Hashimoto, G. L. 2015, *ApJ*, 806, 216
- Hatzes, A. P., Fridlund, M., Nachmani, G., et al. 2011, *ApJ*, 743, 75
- Heng, K. 2012, *ApJ*, 761, L1
- Heng, K., & Kopparla, P. 2012, *ApJ*, 754, 60
- Heng, K., Wyttenbach, A., Lavie, B., et al. 2015, *ApJ*, 803, L9
- Henning, W. G., & Hurford, T. 2014, *ApJ*, 789, 30
- Honda, R., Mizutani, H., & Yamamoto, T. 1993, *J. Geophys. Res.*, 98, 2075
- Howard, A. W., Sanchis-Ojeda, R., Marcy, G. W., et al. 2013, *Nature*, 503, 381
- Howe, A. R., Burrows, A., & Verne, W. 2014, *ApJ*, 787, 173
- Howe, A. R., & Burrows, A. 2015, *ApJ*, 808, 150
- Hu, R., Ehlmann, B. L., & Seager, S. 2012, *ApJ*, 752, 7
- Hu, R., Demory, B.-O., Seager, S., Lewis, N., & Showman, A. P. 2015, *ApJ*, 802, 51
- Hughes, G. O., & Griffiths, R. W. 2008, *Annual Review of Fluid Mechanics*, 40, 185
- Ida, S., Nakagawa, Y., & Nakazawa, K. 1987, *Icarus*, 69, 239
- Ida, S., Nakagawa, Y., & Nakazawa, K. 1989, *Earth Moon and Planets*, 44, 149
- Inamdar, N. K., & Schlichting, H. E. 2015, *MNRAS*, 448, 1751
- Ingersoll, A. P., Summers, M. E., & Schlipf, S. G. 1985, *Icarus*, 64, 375
- Ingersoll, A. P. 1989, *Icarus*, 81, 298
- Ito, Y., Ikoma, M., Kawahara, H., et al. 2015, *ApJ*, 801, 144
- Jackson, B., Greenberg, R., & Barnes, R. 2008, *ApJ*, 681, 1631
- Jakse, N., Bouhadja, M., Kozaily, J., et al. 2012, *Applied Physics Letters*, 101, 201903
- Jessup, K. L., Spencer, J. R., Ballester, G. E., et al. 2004, *Icarus*, 169, 197
- Jin, S., Mordasini, C., Parmentier, V., et al. 2014, *ApJ*, 795, 65
- Jones, A. P. 1990, *MNRAS*, 245, 331
- Juhász, A., Bouwman, J., Henning, T., et al. 2010, *ApJ*, 721, 431
- Jura, M., & Young, E. D. 2014, *AREPS*, 42, 45
- Karato, S.-i., & Rama Murthy, V. 1997, *PEPI*, 100, 61
- Karki, B. B., Bhattarai, D., Mookherjee, M., & Stixrude, L. 2010, *Physics and Chemistry of Minerals*, 37, 103
- Katz, R. F., Spiegelman, M., & Langmuir, C. H. 2003, *GGG*, 4, 1073
- Katz, R. F., Spiegelman, M., & Holtzman, B. 2006, *Nature*, 442, 676
- Keil, K. 2012, *Chemie der Erde / Geochemistry*, 72, 191
- Kite, E. S., Manga, M., & Gaidos, E. 2009, *ApJ*, 700, 1732
- Klein, E.M., *Geochemistry of the Igneous Oceanic Crust*, p. 433-463, in *Treatise on Geochemistry*, vol. 3, 1st edition
- Klein, F., Bach, W., & McCollom, T. M. 2013, *Lithos*, 178, 55
- Korenaga, J. 2013, *AREPS*, 41, 117
- Koskinen, T. T., Yelle, R. V., Lavvas, P., & Y-K. Cho, J. 2014, *ApJ*, 796, 16
- Krzesinski, J. 2015, *A&A*, 581, A7
- Krot, A. N., Fegley, B., Jr., Lodders, K., & Palme, H. 2000, *Protostars and Planets IV*, 1019
- Kuwahara, H., & Sugita, S. 2015, *Icarus*, 257, 290
- Lange, M. A., & Ahrens, T. J. 1984, *E&PSL*, 71, 111
- Lange, R. A., & Carmichael, I. S. E. 1987, *Geochim. Cosmochim. Acta*, 51, 2931
- Lange, R. A., & Carmichael, I. S. E. 1990, *Rev. Mineral. Geochem.*, 24, 25-64
- Lauretta, D. S., Nagahara, H., & Alexander, C. M. O. 2006, *Meteorites and the Early Solar System II*, 431
- Leconte, J., Forget, F., Charnay, B., et al. 2013, *A&A*, 554, A69
- Lee, E. J., Chiang, E., & Ormel, C. W. 2014, *ApJ*, 797, 95
- Léger, A., Rouan, D., Schneider, J., et al. 2009, *A&A*, 506, 287
- Léger, A., Grasset, O., Fegley, B., et al. 2011, *Icarus*, 213, 1
- Lenardic, A., & Crowley, J. f W. 2012, *ApJ*, 755, 132
- Lewis, J., *Physics and Chemistry of the Solar System*, 2nd edition, Academic Press.
- Lodders, K., & Fegley, B. 1998, *The planetary scientist's companion*. New York : Oxford University Press, 1998.
- Lodders, K., Palme, H., & Gail, H.-P. 2009, *Landolt Börnstein*, 44 López-Morales, M., Gómez-Pérez, N., & Ruedas, T. 2011, *OLEB*, 41, 533
- Lissauer, J. J., Dawson, R. I., & Tremaine, S. 2014, *Nature*, 513, 336
- Lopez, E. D., & Fortney, J. J. 2014, *ApJ*, 792, 1
- Lorenz, R. D., & Hayes, A. G. 2012, *Icarus*, 219, 468
- Lupu, R. E., Zahnle, K., Marley, M. S., et al. 2014, *ApJ*, 784, 27
- Makarov, V. V., & Efroimsky, M. 2013, *ApJ*, 764, 27
- Makarov, V. V., & Efroimsky, M. 2014, *ApJ*, 795, 7
- Makarov, V. V. 2015, *ApJ*, 810, 12
- McCollom, T. M., & Bach, W. 2009, *Geochim. Cosmochim. Acta*, 73, 856
- McCord, T. B., & Sotin, C. 2005, *JGR-Planets*, 110, E05009
- McDonough, W. F., & Sun, S. 1995, *Chemical Geology*, 120, 223
- Mills, K. C., Hayashi, M., Wang, L., & Watanabe, T., 2014, *Treatise on Process Metallurgy*, vol. 1., Chapter 2.2.
- Min, M., Waters, L. B. F. M., de Koter, A., et al. 2007, *A&A*, 462, 667
- Miyagoshi, T., Tachinami, C., Kameyama, M., & Ogawa, M. 2014, *ApJ*, 780, L8
- Morgan, J. W., & Anders, E. 1980, *PNAS*, 77, 6973
- Moore, W. B., Schubert, G., Anderson, J. D., & Spencer, J. R. 2007, *Io After Galileo: A New View of Jupiter's Volcanic Moon*, 89
- Moore, W. B., & Webb, A. A. G. 2013, *Nature*, 501, 501

- Moutou, C., Deleuil, M., Guillot, T., et al. 2013, *Icarus*, 226, 1625
- Moynier, F., & Fegley, B., pp. 27-47 *in* The Early Earth: Accretion & Differentiation, AGU Geophys. Monograph 212.
- Munk, W., & Wunsch, C. 1998, *Deep Sea Research Part I*, 45, 1977
- Murray-Clay, R. A., Chiang, E. I., & Murray, N. 2009, *ApJ*, 693, 23
- Ni, H., Hui, H., & Steinle-Neumann, G., 2015, *Rev. Geophys.*, 53, doi:10.1002/2015RG000485.
- Nikolov, N., Sing, D. K., Pont, F., et al. 2014, *MNRAS*, 437, 46
- Noack, L., Godolt, M., von Paris, P., et al. 2014, *Planet. Space Sci.*, 98, 14
- Nowack, N. 2001, *J. of Non Crystalline Solids*, 282, 30
- Ogihara, M., Morbidelli, A., & Guillot, T. 2015, *A&A*, 578, A36
- Öpik, E.J, 1958, *Physics of Meteor Flight in the Atmosphere* (Dover Phoenix Editions).
- O'Rourke, J. G., & Korenaga, J. 2012, *Icarus*, 221, 1043
- Owen, J. E., & Jackson, A. P. 2012, *MNRAS*, 425, 2931
- Owen, J. E., & Wu, Y. 2013, *ApJ*, 775, 105
- Owen, J. E., & Alvarez, M. A. 2015, arXiv:1504.07170
- Owen, J. E., & Morton, T. D. 2016, *ApJ*, 819, L10
- Ozawa, K., & Nagahara, H. 1997, *Proc. LPSC*, 28, 1055
- Ozawa, K., & Nagahara, H. 2001, *Geochim. Cosmochim. Acta*, 65, 2171
- Pepe, F., Cameron, A. C., Latham, D. W., et al. 2013, *Nature*, 503, 377
- Perez-Becker, D., & Chiang, E. 2013, *MNRAS*, 433, 2294
- Petrov, V. A. 2009, *International J. of Thermophysics*, 30, 1938
- Podolak, M., & Zucker, S. 2004, *M&PS*, 39, 1859
- Rappaport, S., Levine, A., Chiang, E., et al. 2012, *ApJ*, 752, 1
- Rappaport, S., Sanchis-Ojeda, R., Rogers, L. A., Levine, A., & Winn, J. N. 2013, *ApJ*, 773, L15
- Rappaport, S., Barclay, T., DeVore, J., et al. 2014, *ApJ*, 784, 40
- Rauscher, E., & Menou, K. 2013, *ApJ*, 764, 103
- Raymond, S. N., Kokubo, E., Morbidelli, A., Morishima, R., & Walsh, K. J. 2014, *Protostars and Planets VI*, 595
- Reese, C. C., & Solomatov, V. S. 2006, *Icarus*, 184, 102
- Reilman, R. F., & Manson, S. T. 1979, *ApJS*, 40, 815
- Richter, F. M., Davis, A. M., Ebel, D. S., & Hashimoto, A. 2002, *Geochim. Cosmochim. Acta*, 66, 521
- Richter, F. M. 2004, *Geochim. Cosmochim. Acta*, 68, 4971
- Richter, F. M., Janney, P. E., Mendybaev, R. A., Davis, A. M., & Wadhwa, M. 2007, *Geochim. Cosmochim. Acta*, 71, 5544
- Richter, F. M., Mendybaev, R. A., Christensen, J. N., Ebel, D., & Gaffney, A. 2011, *M&PS*, 46, 1152
- Righter, K., & Drake, M. J. 1997, *M&PS*, 32, 929
- Rizo, H., et al., 2016, *Science*, doi:10.1126/science.aad8563
- Rogers, L. A., & Seager, S. 2010, *ApJ*, 712, 974
- Rogers, L. A., Bodenheimer, P., Lissauer, J. J., & Seager, S. 2011, *ApJ*, 738, 59
- Rogers, L. A. 2015, *ApJ*, 801, 41
- Rouan, D., Deeg, H. J., Demangeon, O., et al. 2011, *ApJ*, 741, L30
- Rosenberg, N. D., Browning, L., & Bourcier, W. L. 2001, *M&PS*, 36, 239
- Rossby, H. T. 1965, *Deep Sea Research*, 12, 9
- Rubie, D. C., Frost, D. J., Mann, U., et al. 2011, *E&PSL*, 301, 31
- Rubie, D. C., Jacobson, S. A., Morbidelli, A., et al. 2015, *Icarus*, 248, 89
- Russell, J.K, Giordano, D., Dingwell, D.B., 2003, *American Mineralogist*, 88, 1390
- Samuel, B., Lecointe, J., Rouan, D., et al. 2014, *A&A*, 563, A103
- Sanchis-Ojeda, R., Rappaport, S., Pallè, E., et al. 2015, *ApJ*, 812, 112
- Sandström, J.W.. 1908, *Annalender Hydrographie under Martimen Meteorologie*, 6, 6-23
- Schlichting, H. E. 2014, *ApJ*, 795, L15
- Schlichting, H. E., Sari, R., & Yalinewich, A. 2015, *Icarus*, 247, 81
- Scott, D. R., & Stevenson, D. J. 1984, *Geophys. Res. Lett.*, 11, 1161
- Stommel, H. 1961, *Tellus* 13, 131 (S61).
- Schaefer, L., & Fegley, B. 2004, *Icarus*, 169, 216
- Schaefer, L., & Fegley, B. 2009, *ApJ*, 703, L113
- Schaefer, L., & Fegley, B. 2010, *Icarus*, 208, 438
- Schaefer, L., Lodders, K., & Fegley, B. 2012, *ApJ*, 755, 41
- Schlawin, E., et al., 2016, arXiv:1605.07603
- Seager, S., Kuchner, M., Hier-Majumder, C. A., & Militzer, B. 2007, *ApJ*, 669, 1279
- Sharp, Z. D., McCubbin, F. M., & Shearer, C. K. 2013, *E&PSL*, 380, 88
- Sheets, H. A., & Deming, D. 2014, *ApJ*, 794, 133
- Showman, A. P., Cho, J. Y.-K., & Menou, K. 2010, *in* S. Seager (Ed.), *Exoplanets*, 471-
- Sleep, N. H. 2000, *J. Geophys. Res.*, 105, 17563
- Sleep, N. H., Meibom, A., Fridriksson, T., Coleman, R. G., & Bird, D. K. 2004, *PNAS*, 101, 12818
- Sleep, N. 2007, chapter 9.06, *in* *Treatise on Geophysics* (1st edition), vol. 9.
- Solomatov, S. 2015, chapter 9.04, *in* *Treatise on Geophysics* (2nd edition), vol. 9.
- Stamenković, V., & Breuer, D. 2014, *Icarus*, 234, 174
- Suckale, J., Elkins-Tanton, L. T., & Sethian, J. A. 2012, *Journal of Geophysical Research (Planets)*, 117, E08005
- Sullivan, P. W., Winn, J. N., Berta-Thompson, Z. K., et al. 2015, *ApJ*, 809, 77
- Swift, D. C., Eggert, J. H., Hicks, D. G., et al. 2012, *ApJ*, 744, 59
- Tackley, P. J., Ammann, M., Brodholt, J. P., Dobson, D. P., & Valencia, D. 2013, *Icarus*, 225, 50
- Takahashi, E. 1986, *J. Geophys. Res.*, 91, 9367
- Taylor, S. R., & McLennan, S. 2009, *Planetary Crusts*, Cambridge University Press.
- Tian, F., Kasting, J. F., & Solomon, S. C. 2009, *Geophys. Res. Lett.*, 36, L02205.
- Tian, F. 2015, *AREPS*, 43, 459
- Thiabaud, A., Marboeuf, U., Alibert, Y., Leya, I., & Mezger, K. 2015, *A&A*, 580, A30
- Tokano, T., & Lorenz, R. D. 2016, *Icarus*, 270, 67
- Tsuchiyama, A., Kawamura, K., Nakao, T., & Uyeda, C. 1994, *Geochim. Cosmochim. Acta*, 58, 3013
- Tsuchiyama, A., Tachibana, S., & Takahashi, T. 1999, *Geochim. Cosmochim. Acta*, 63, 2451
- Tyler, R. H., Henning, W. G., & Hamilton, C. W. 2015, *ApJS*, 218, 22
- Valencia, D., Ikoma, M., Guillot, T., & Nettelmann, N. 2010, *A&A*, 516, A20
- Vallis, G. 2006, *Atmospheric and oceanic fluid dynamics*, Cambridge University Press.
- Vanderburg, A., Johnson, J. A., Rappaport, S., et al. 2015, arXiv:1510.06387
- van Lieshout, R., Min, M., & Dominik, C. 2014, *A&A*, 572, A76
- Van Orman, J.A., and Crispin, K.L., *Diffusion in Oxides*, pp. 757-825, *in* *Rev. Mineral. Geochem.*, 72, 2010.
- van Summeren, J., Conrad, C. P., & Gaidos, E. 2011, *ApJ*, 736, L15
- van Werkhoven, T. I. M., Brogi, M., Snellen, I. A. G., & Keller, C. U. 2014, *A&A*, 561, A3
- Wade, J., & Wood, B. J. 2005, *E&PSL*, 236, 78
- Walker, A. C., Gratiy, S. L., Goldstein, D. B., et al. 2010, *Icarus*, 207, 409
- Walker, A. C., Moore, C. H., Goldstein, D. B., Varghese, P. L., & Trafton, L. M. 2012, *Icarus*, 220, 225
- Wang, J., Davis, A. M., & Clayton, R. N. 1994, *Abstracts of the Eighth International Conference on Geochronology*, p. 348.
- Watters, W. A., Zuber, M. T., & Hager, B. H. 2009, *JGR-Planets*, 114, E02001
- Weiss, L. M., & Marcy, G. W. 2014, *ApJ*, 783, L6
- Wilson, H. F., & Militzer, B. 2014, *ApJ*, 793, 34
- Wolfgang, A., & Lopez, E. 2015, *ApJ*, 806, 183
- Wolfgang, A., Rogers, L. A., & Ford, E. B. 2015, arXiv:1504.07557
- Wordsworth, R. 2015, *ApJ*, 806, 180
- Wu, Y., & Lithwick, Y. 2013, *ApJ*, 772, 7
- Wunsch, C. 2005, *Tellus Series A*, 57, 84
- Wytttenbach, A., Ehrenreich, D., Lovis, C., Udry, S., & Pepe, F. 2015, *A&A*, 577, A62
- Zahnle, K.J., Catling, D.C., & Claire, M.W. 2013, *Chemical Geology*, 362, 26
- Zahnle, K. J., Lupu, R., Dobrovolskis, A., & Sleep, N. H. 2015, *E&PSL*, 427, 74
- Zebger, I., Pfeifer, F., & Nowack, N. 2005, *J. of Non Crystalline Solids*, 351, 3443
- Zolotov, M. Y., Sprague, A. L., Hauck, S. A., et al. 2013, *JGR-Planets*, 118, 138